Miner Deposita (2017) 52:565–593
DOI 10.1007/s00126-016-0680-x

ARTICLE

Geochemistry of host rocks in the Howards Pass district, Yukon-Northwest Territories, Canada: implications for sedimentary environments of Zn-Pb and phosphate mineralization

John F. Slack[1] · **Hendrik Falck**[2] · **Karen D. Kelley**[3] · **Gabriel G. Xue**[4]

Received: 29 March 2016 / Accepted: 26 August 2016 / Published online: 5 October 2016

Abstract Detailed lithogeochemical data are reported here on early Paleozoic sedimentary rocks that host the large Howards Pass stratiform Zn-Pb deposits in Yukon-Northwest Territories. Redox-sensitive trace elements (Mo, Re, V, U) and Ce anomalies in members of the Duo Lake Formation record significant environmental changes. During the deposition of lower footwall units (Pyritic siliceous and Calcareous mudstone members), bottom waters were anoxic and sulphidic, respectively; these members formed in a marginal basin that may have become increasingly restricted with time. Relative to lower members, a major environmental change is proposed for deposition of the overlying Lower cherty mudstone member, which contains phosphorite beds up to ~0.8 m thick in the upper part, near the base of the Zn-Pb deposits. The presence of these beds, together with models for modern phosphorite formation, suggests P input from an upwelling system and phosphorite deposition in an upper slope or outer shelf setting. The overlying Active mudstone member contains stratabound to stratiform Zn-Pb deposits within black mudstone and gray calcareous mudstone. Data for unmineralized black mudstone in this member indicate deposition under diverse redox conditions from suboxic to sulphidic. Especially distinctive in this member are uniformly low ratios of light to heavy rare earth elements that are unique within the Duo Lake Formation, attributed here to the dissolution of sedimentary apatite by downward-percolating acidic metalliferous brines. Strata that overlie the Active member (Upper siliceous mudstone member) consist mainly of black mudstone with thin (0.5–1.5 cm) laminae of fine-grained apatite, recording continued deposition on an upper slope or outer shelf under predominantly suboxic bottom waters. Results of this study suggest that exploration for similar stratiform sediment-hosted Zn-Pb deposits should include the outer parts of ancient continental margins, especially at and near stratigraphic transitions from marginal basin facies to overlying slope or shelf facies.

Keywords Howards Pass · Yukon · Northwest Territories · Zn-Pb deposits · Early Paleozoic · Black mudstone · Phosphorite · Lithogeochemistry · Paleoredox · Upwelling · Sedimentary environments

Editorial handling: B. Lehmann

Electronic supplementary material The online version of this article (doi:10.1007/s00126-016-0680-x) contains supplementary material, which is available to authorized users.

✉ John F. Slack
jfslack@usgs.gov

[1] U.S. Geological Survey, National Center, MS 954, Reston, VA 20192, USA

[2] NWT Geoscience Office, P.O. Box 1320, Yellowknife, NWT X1A 2L9, Canada

[3] U.S. Geological Survey, Denver Federal Center, MS 973, Denver, CO 80225, USA

[4] Selwyn Chihong Mining Ltd., 2701-1055 West Georgia St, Vancouver, BC V6E 0B6, Canada

Introduction

One of the major uncertainties in genetic models for sediment-hosted stratiform Zn-Pb deposits is whether the base-metal mineralization is chiefly of syngenetic or epigenetic origin (e.g., Leach et al. 2005; Wilkinson 2014). Many workers have assumed that these deposits formed chiefly by syngenetic processes, i.e., directly on the seafloor coeval with sedimentation. However, numerous textural, geochemical, and isotopic

studies have provided compelling evidence for an early or late diagenetic deposition of the base-metal sulphides. Examples include Paleoproterozoic deposits at HYC (Chen et al. 2003) and Century in Queensland (Broadbent et al. 1998), Devonian deposits at Tom and Jason in Yukon Territory (Magnall et al. 2016), and Mississippian deposits at Red Dog and Anarraaq in Alaska (Kelley et al. 2004a, b; Johnson et al. 2015). Although the current state of knowledge does not rule out, a priori, a syngenetic model for a specific deposit, a growing consensus is that predominantly syngenetic-exhalative mineralization is uncommon during the formation of sediment-hosted stratiform Zn-Pb deposits (Leach et al. 2005; Wilkinson 2014). Leach et al. (2010) adopted the term clastic-dominated Pb-Zn (CD Pb-Zn) as a descriptive classification for a class of predominantly stratiform deposits that formed by syngenetic and/or diagenetic processes; this term is used herein.

A related issue in the syngenetic-epigenetic debate is the redox state of bottom waters during mineralization. Redox conditions are key factors to evaluate because anoxic or sulphidic (euxinic) bottom waters are generally considered a prerequisite for exhalative deposition by providing a large fluid reservoir of H_2S for sulphide formation and by excluding dissolved O_2 that would promote the oxidation of sulphide minerals on the sea floor (e.g., Goodfellow 1987; Kříbek 1991; Turner 1992). Previous geochemical studies have proposed anoxic or sulphidic bottom waters for some deposits, including the Mesoproterozoic Sullivan orebody in British Columbia (Goodfellow 2000), the Ordovician Citronen Fjord deposit in North Greenland (Slack et al. 2015b), the Devonian Tharsis deposit in Spain (Sáez et al. 2011), and the Devonian Tom and Jason deposits in Yukon (Goodfellow 2007; cf. Magnall et al. 2016). In contrast, a range of bottom-water conditions from sulphidic to oxic has been suggested for host rocks of the Mississippian Red Dog and Anarraaq deposits (Slack et al. 2004a; Johnson et al. 2015). It is important to emphasize, however, that if a late diagenetic (or metamorphic) timing of mineralization can be demonstrated for a sediment-hosted Zn-Pb deposit, then the redox state of bottom waters during the deposition of immediately underlying and overlying strata is not directly relevant. However, anoxic or sulphidic redox states of such waters could be important for very early diagenetic mineralization—occurring within unlithified sediments—based on evidence for the downward migration of reduced bottom waters into Fe-limited sediments of late Pleistocene age in the Cariaco Basin (Lyons et al. 2003).

In this report, we use whole-rock geochemistry to evaluate bottom-water redox conditions and local sedimentary environments during formation of the XY Central (XYC) Zn-Pb deposit in the Howards Pass district of eastern Yukon and adjoining Northwest Territories. Both parameters are emphasized in the context of recent studies by Gadd et al. (2016b, 2016c) based on microtextural and laser ablation ICP-MS data and in situ sulphur isotope analyses, which collectively provide strong evidence of syngenetic to early diagenetic Zn-Pb mineralization in the district. Therefore, efforts to constrain paleoredox conditions at Howards Pass during sedimentation are meaningful. In addition to lithogeochemistry of the host sedimentary rocks, our study is supported by petrography, scanning electron microscopy (SEM), X-ray diffraction (XRD), and electron probe microanalysis (EPMA). Integration of these data, together with insights from modern and ancient sedimentary realms, is used here as a basis for re-evaluating the sedimentary environments of the Howards Pass Zn-Pb district and for providing applications to mineral exploration in the region and elsewhere.

Geological setting

The Howards Pass Zn-Pb district is mainly in easternmost Yukon Territory with an extension into adjacent Northwest Territories (Fig. 1). This district is within the Neoproterozoic to Devonian Selwyn Basin that contains stratiform sediment-hosted Zn-Pb and barite deposits, adjacent to the Mackenzie carbonate platform (Cambrian-Devonian) that hosts stratabound Mississippi Valley-type (MVT) deposits (e.g., Goodfellow 2007). The Howards Pass district forms a northwest-trending belt that extends at least 38 km along strike and contains 15 separate Zn-Pb zones (Fig. 2). All major sulphide zones occur within the Duo Lake Formation of the Ordovician to Silurian Road River Group (Fig. 3). Basal strata in this part of the Selwyn Basin, stratigraphically far below the Duo Lake (Gordey and Anderson 1993), are shale and minor sandstone of the Neoproterozoic to Cambrian Narchilla Formation. Similar siliciclastic lithologies, together with minor limestone, occur in the overlying Gull Lake Formation of Cambrian age. Above this succession and directly below the Duo Lake is limestone of the Cambrian Rabbitkettle Formation, overlain by a transition unit that Hodder et al. (2014) interpreted as a major regional décollement zone. No volcanic rocks are known within the Duo Lake Formation in the district, but volumetrically minor alkalic and potassic basalts occur in correlative strata elsewhere in the Selwyn Basin (Goodfellow et al. 1995 and references therein).

Morganti (1979) proposed stratigraphic subdivisions in the district that have been followed by all subsequent workers. These subdivisions are used herein, but the informally named Howards Pass formation is not. Hodder et al. (2014) estimated that in the district, the Duo Lake Formation varies in thickness from 230 to 300 m. The lowermost unit is the Pyritic siliceous mudstone member (Fig. 3), 2 to 10 m thick, consisting of dark gray to black dolomitic mudstone, with pyrite concretions and thin pyrite laminae; dolomite is common based on this study

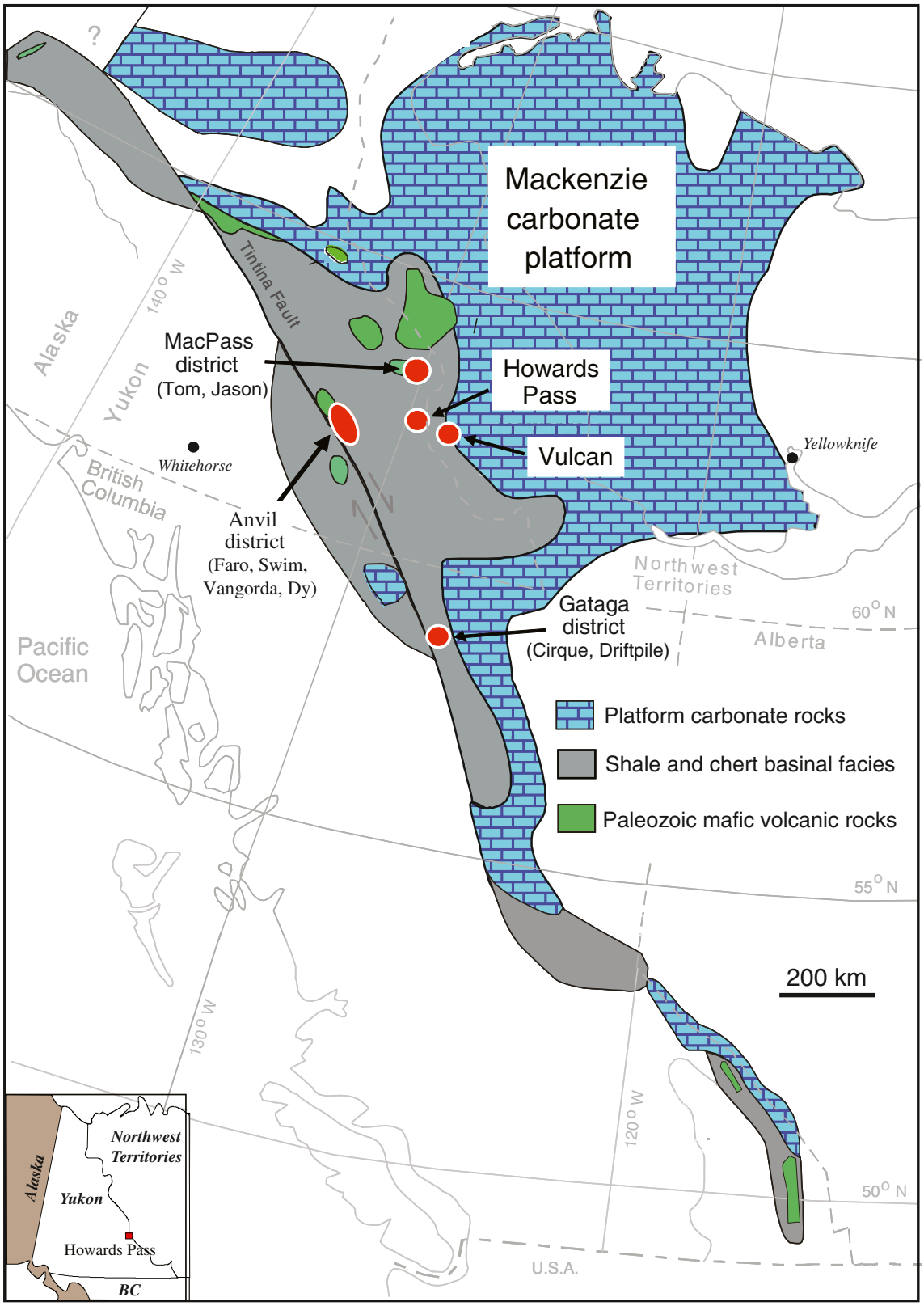

Fig. 1 Generalized map showing Mackenzie Platform and time-equivalent shale and chert facies of Selwyn Basin. Clastic-dominated Zn-Pb (CD Zn-Pb) deposits of Howards Pass district are immediately west of carbonate platform. Other significant Pb-Zn districts of Paleozoic age include MacMillan Pass (Tom and Jason deposits), Anvil (Faro, Swim, Vangorda, and Dy deposits), and Gataga (Cirque and Driftpile deposits). Modified from Goodfellow (2007)

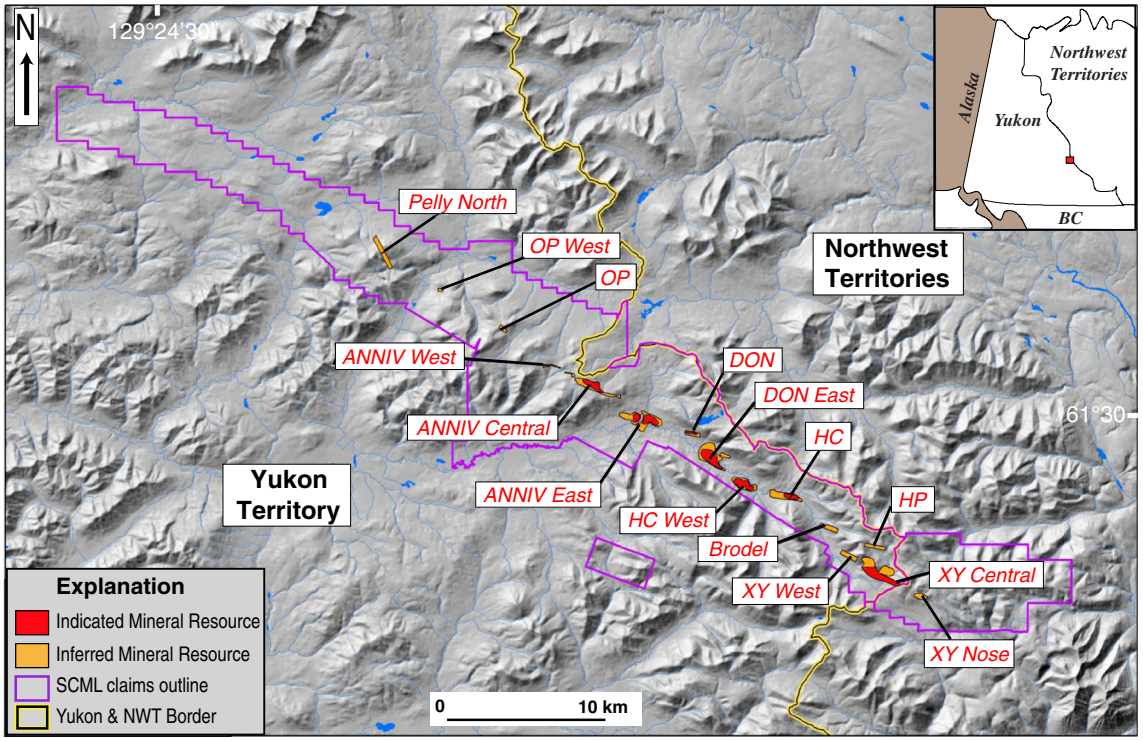

Fig. 2 Simplified map of Howards Pass district on border between Yukon and Northwest Territories. At least 15 mineralized centers occur along a northwest-trending belt. Samples used for this study were collected from XY Central (XYC) and DON deposits. *SCML* Selwyn Chihong Mining Ltd. Modified rom Kirkham et al. (2012)

(not reported by previous workers). Above this member is the Calcareous carbonaceous mudstone member (50–100 m), which comprises dark gray, typically carbonaceous and calcareous mudstone (in places with minor K-feldspar and hyalophane; Goodfellow and Jonasson 1986), and the Lower cherty mudstone member (15–30 m) composed chiefly of black carbonaceous mudstone with phosphorite beds locally near the top. The overlying Active member, commonly 20 to 30 m thick, hosts nearly all known Zn-Pb zones in the district and contains sphalerite and galena with minor pyrite, black mudstone, and chert; highly siliceous rock is present near the top. Phosphorite occurs locally at and near the base. Above the Active member is the Upper siliceous mudstone member (20–90 m), which comprises gray to black mudstone typically with thin (0.5–1.5 cm) beds of very fine-grained phosphorite and minor limestone, with local pyrite-rimmed carbonate concretions up to 1 m in diameter (Goodfellow 2007). The lower part of the upper siliceous mudstone member also contains highly siliceous beds. Overlying the Duo Lake is the Upper Silurian Flaggy mudstone member (Morganti 1979) of the Steel Formation, 100 to 140 m thick, consisting mainly of gray dolomitic mudstone with distinctive bioturbated structures (Morganti 1979; Gordey and Anderson 1993). The Flaggy mudstone member is overlain by the Backside siliceous mudstone member of the lower Portrait Lake Formation (Earn Group).

Ages of the stratigraphic units are based on graptolites and conodonts (see summary in Kelley et al. 2016, Fig. 9). Graptolites from the Duo Lake Formation regionally range in age from Early Ordovician to late Silurian (Gordey and Anderson 1993). No faunal age is available for the Pyritic siliceous mudstone member. Graptolites in the overlying Calcareous carbonaceous mudstone member and near the top of the Upper siliceous mudstone member are Late Ordovician and middle Silurian, respectively (Morganti 1979). Conodonts in the Active member are early Llandovery (Norford and Orchard 1985), which correlates with the early Silurian range of 441 to 439 Ma using the time scale of Gradstein et al. (2012). The age of the Flaggy mudstone member is poorly constrained but is in part late Ludow based on graptolites from outside the Howards Pass district (Gordey and Anderson 1993). Conodonts at seven localities northwest of the district yield Late Ordovician to early Silurian ages and have conodont alteration indices (CAI) of 4.5 to 5.0 (McCracken 2014), the latter reflecting burial temperatures of ca. 300 to 400 °C (see Rejebian et al. 1987). Within the district, conodonts from the Duo Lake Formation are uniformly black and suggest a similar temperature range (Norford and Orchard 1985).

The structure of the Howards Pass district is more complex than described by early workers. Detailed structural mapping throughout the district by Hodder et al. (2014) and Martel (2015) indicates that much of the local succession is cut by district-scale thrust faults, with the result that simple application of the long-standing stratigraphic framework (Fig. 3) is locally problematic, especially where parts of units have been repeated

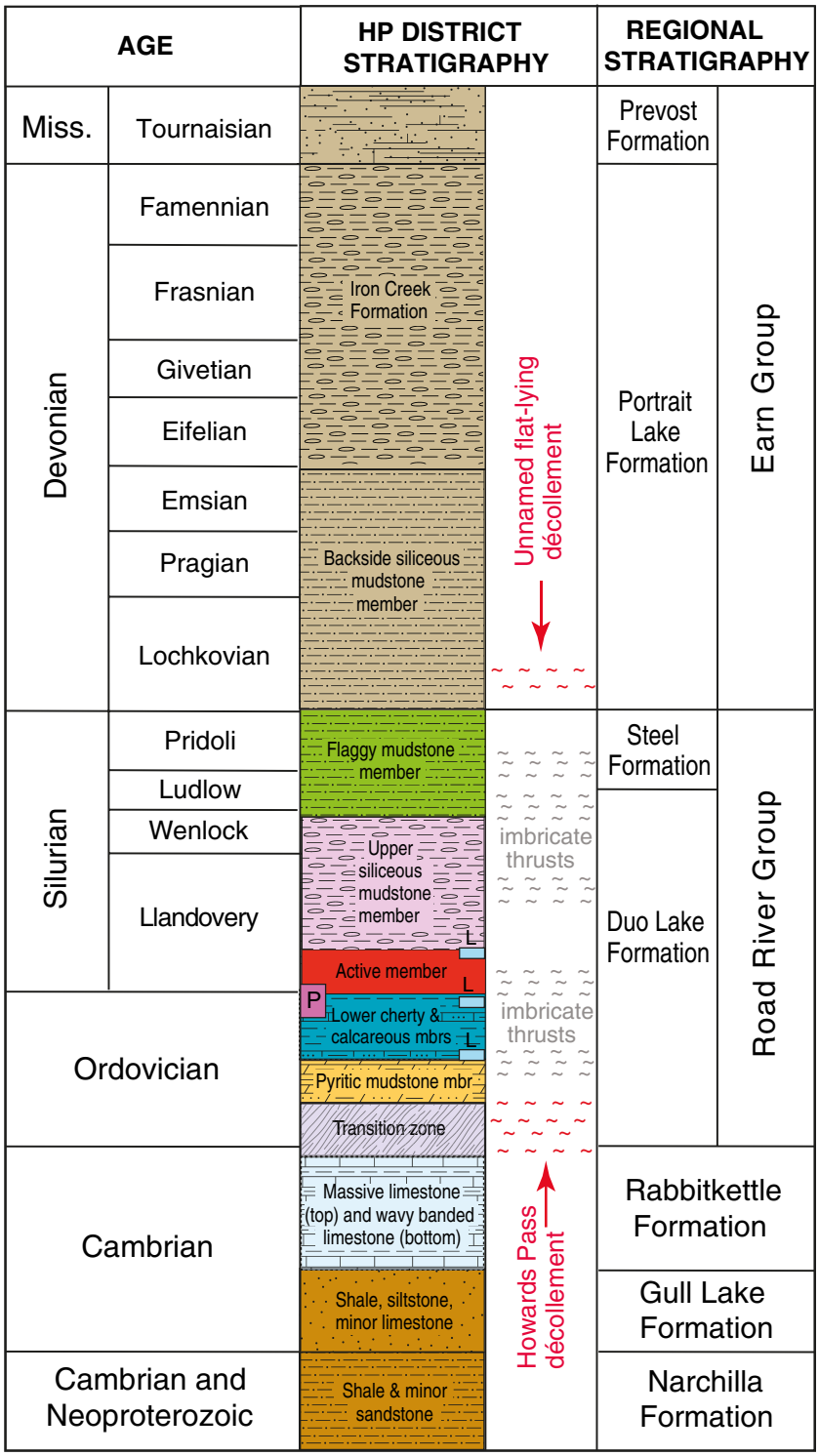

Fig. 3 Stratigraphic column of Selwyn Basin in Howards Pass district (modified from Morganti 1979; Gordey and Anderson 1993; Goodfellow 2007). No vertical scale is implied. Thicknesses of formations and members are given in text; ages are based on graptolites and conodonts (Morganti 1979; Norford and Orchard 1985). Active member of Duo Lake Formation contains all major mineralized zones in Howards Pass district. *L* limestone, *P* phosphorite. Recent mapping by Hodder et al. (2014) reveals complexity of deformation that includes a major flat-lying décollement (*red wavy lines*) at top of Rabbitkettle Formation and imbricate thrust faults (*gray wavy lines*) occurring in parts of Duo Lake Formation

or removed by faulting. Deformation took place during Early to Middle Cretaceous docking of western (present coordinates) allochthonous terranes with the North America continent (Gordey and Anderson 1993). In addition to thrust faults, deformation in the district produced folds, duplex structures, and local mylonite zones; a late cleavage is also present (Hodder et al. 2014; Martel

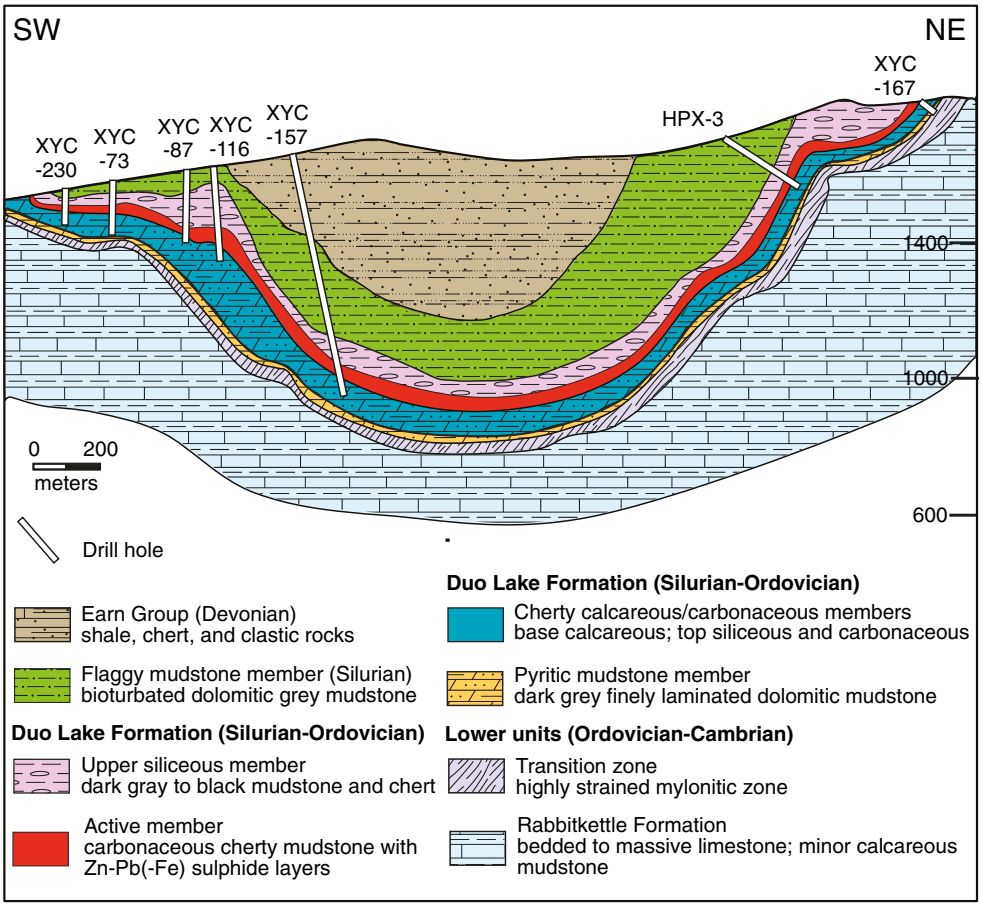

Fig. 4 Geologic cross section of XYC deposit showing stratiform nature of Zn-Pb sulphide zone (Active member) within a broad synclinal structure. Locations of analyzed drill cores XYC-116 and XYC-167 are indicated. Note that position of XYC-167 is schematic, projected from 1640 m east of the section. From Selwyn Chihong Mining Ltd.

2015). Some deposits such as XYC (Fig. 4) and DON are relatively undeformed. Significantly, whereas previous studies attributed the northwest-trending belt of Zn-Pb deposits in the district to mineralization in separate depositional basins (e.g., Morganti 1979; Goodfellow and Jonasson 1986; Goodfellow 2007), the recent work by Hodder et al. (2014) suggests that this alignment of deposits is a structural artifact of the surface traces of parallel, southwest-dipping thrust faults.

Zn-Pb deposits

Exploration history and deposit styles

Exploration work in the late 1960s by Placer Development Ltd. culminated in the 1972 discovery of Zn-Pb deposits. This discovery was guided by stream-sediment geochemical anomalies and the subsequent identification of base-metal showings in outcrops. Drilling programs began in 1973 and continued until 1979. From 2005 to 2012, extensive new drilling and exploration by Selwyn Resources Ltd. (formerly Pacifica Resources Ltd.) and Selwyn Chihong Mining Ltd. delineated total (district-scale) indicated resources of 185.6 Mt at 5.20 % Zn and 1.79 % Pb and inferred resources of 237.9 Mt at 4.47 % Zn and 1.38 % Pb (Kirkham et al. 2012). The XYC deposit is the largest known in the district, containing 45.1 Mt of indicated resources at 5.7 % Zn and 2.4 % Pb and 44.1 Mt of inferred resources at 4.10 % Zn and 1.29 % Pb. On a global scale, the 26.9 Mt of total Zn + Pb resources in the Howards Pass district is one of the largest known within the class of sediment-hosted stratiform Zn-Pb deposits (Goodfellow 2007; Leach et al. 2010).

The Zn-Pb deposits form isolated lenses of massive to semimassive sphalerite and galena, typically accompanied by minor pyrite. Individual deposits are tens to hundreds of meters wide and up to 60 m thick. Layers composed of abundant sphalerite and galena are typically intercalated with black mudstone or, less commonly, gray siliceous mudstone or chert. With few exceptions, elevated contents of Zn and Pb (>2 % combined) are restricted to the Active member. However, drill core logs and assay data show base-metal concentrations of ~1–2 % Zn + Pb locally in the uppermost part of the underlying Lower cherty mudstone member and below in the Calcareous carbonaceous mudstone member. Within the XYC deposit, abundant sphalerite and/or galena occur in thin intervals of hangingwall strata above

the Active member. Examples include the middle part of the Upper siliceous mudstone member that has up to 7 % Zn over 0.5 m intervals, and much higher stratigraphically in the upper part of the Backside siliceous mudstone member (lower Portrait Lake Formation), which locally contains laminated sphalerite and galena (Gadd et al. 2016b). However, it is uncertain if these occurrences of high Zn-Pb contents in the footwall and hangingwall members are primary, or instead represent thrust repetitions of mineralized intervals derived from the Active member.

Mineralogy and textures

Based on petrographic studies (Jonasson and Goodfellow 1986; Goodfellow and Jonasson 1986; Gadd et al. 2016b), ore minerals in the Active member of the Howards Pass deposits are dominantly sphalerite with lesser galena and pyrite and rare chalcopyrite. Pyrrhotite, millerite, and molybdenite occur in trace amounts. Gangue constituents include quartz, organic matter, minor carbonate, and sparse illite/smectite. Barite has not been reported from the Zn-Pb zones. Beds and laminae of black mudstone intercalated between sulphide layers consist mainly of quartz, illite-smectite, and organic matter, together with minor carbonate and pyrite. Apatite is generally rare but is locally abundant near the stratigraphic base of the Active member. In domains of minimal deformation, sphalerite and galena form bedding-parallel laminations up to several centimeters thick, typically interspersed with black mudstone and 0.1- to 1-cm-thick laminae composed of framboidal pyrite ~3 to 25 μm in diameter (Fig. 5a; Jonasson and Goodfellow 1986; Gadd et al. 2016b). Some laminae consist of graded framboids (Jonasson and Goodfellow 1986). Pyrite also forms isolated framboids having a large size range (~5–50 μm), aggregates of framboids, and euhedral grains 1 μm to 0.5 cm in diameter. Pyrite replaces, to varying extents, algal structures, sponge spicules, and radiolarians (Jonasson and Goodfellow 1986). Black mudstones within underlying and overlying members of the Duo Lake Formation contain similar size ranges of framboidal and euhedral pyrite, although pyrite in these units is generally minor (<3 vol%) relative to that in the Active member. Pyrite nodules 0.5 cm to several centimeters in diameter, which occur throughout the Duo Lake Formation, display radial or herringbone textures and consist solely of pyrite or contain abundant silicate inclusions (Gadd et al. 2016b). Where early textures are best preserved, sphalerite forms small (~10 to 50 μm) grains within bedding-parallel laminae, typically intercalated with pyrite framboids (Jonasson and Goodfellow 1986).

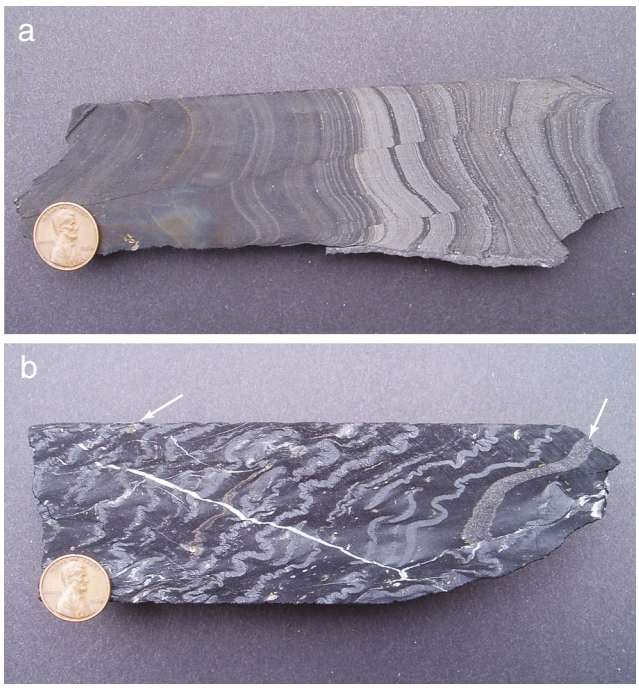

Fig. 5 Photographs of drill core samples. **a** Finely laminated pyrite with minor sphalerite and sparse galena (white) in black mudstone, from middle of Active member, DDH DON-111-123.3 m. **b** Thin contorted laminae of apatite (light) in dark organic-rich mudstone, from upper part of Upper siliceous mudstone member, DDH XYC-116-225.0 m. *Left* and *right* arrows indicate pyrite veinlets and disseminations in thin limestone beds, respectively. Coin is 1.9 cm in diameter

Deformational features are widespread in rocks of the district including sulphide zones of the Active member (Jonasson and Goodfellow 1986; McClay 1991; Hodder et al. 2014; Gadd et al. 2016b). The sulphides and related gangue display a variety of post-sedimentation structures and textures. Recrystallization increased grain sizes, especially for pyrite, by forming layers of coarse crystals and euhedral rims on framboidal pyrite aggregates. Other documented features within the sulphide zones are intrafolial folds, truncated beds, shears, attenuated laminae, cleavage, dilational and crack-seal veins, boudinage, and diapirs; prominent galena-rich veins are localized in the axial surfaces of small-scale folds. In many areas, sphalerite and galena occur in very fine-grained sulphide veins and pressure-solution seams that cut bedding in diverse styles (Gadd et al., 2016b); some discordant galena- and sphalerite-rich seams are probable mylonites (this study; Kelley et al. 2016).

Phosphate and phosphorite

Early studies of the Howards Pass deposits described thin beds and laminae of phosphate (apatite) in hangingwall strata above the Zn-Pb zones (Goodfellow et al. 1983; Goodfellow and Jonasson 1986). These apatite laminae characterize much of the Upper siliceous mudstone member, forming thin (0.5–1.5 cm) beds of very fine-grained apatite that display small-scale, ptygmatic folds (Fig. 5b). Organic-rich mudstone immediately below or above the apatite laminae locally contains thin (1–2 cm) beds of gray limestone with disseminations, rims, and fracture fillings of late pyrite. Although not visible in hand specimen, in detail the laminae have a detrital texture defined by angular grains or fragments of apatite typically <200 μm in diameter with inclusions of calcite, quartz, or organic matter, set in a quartz or

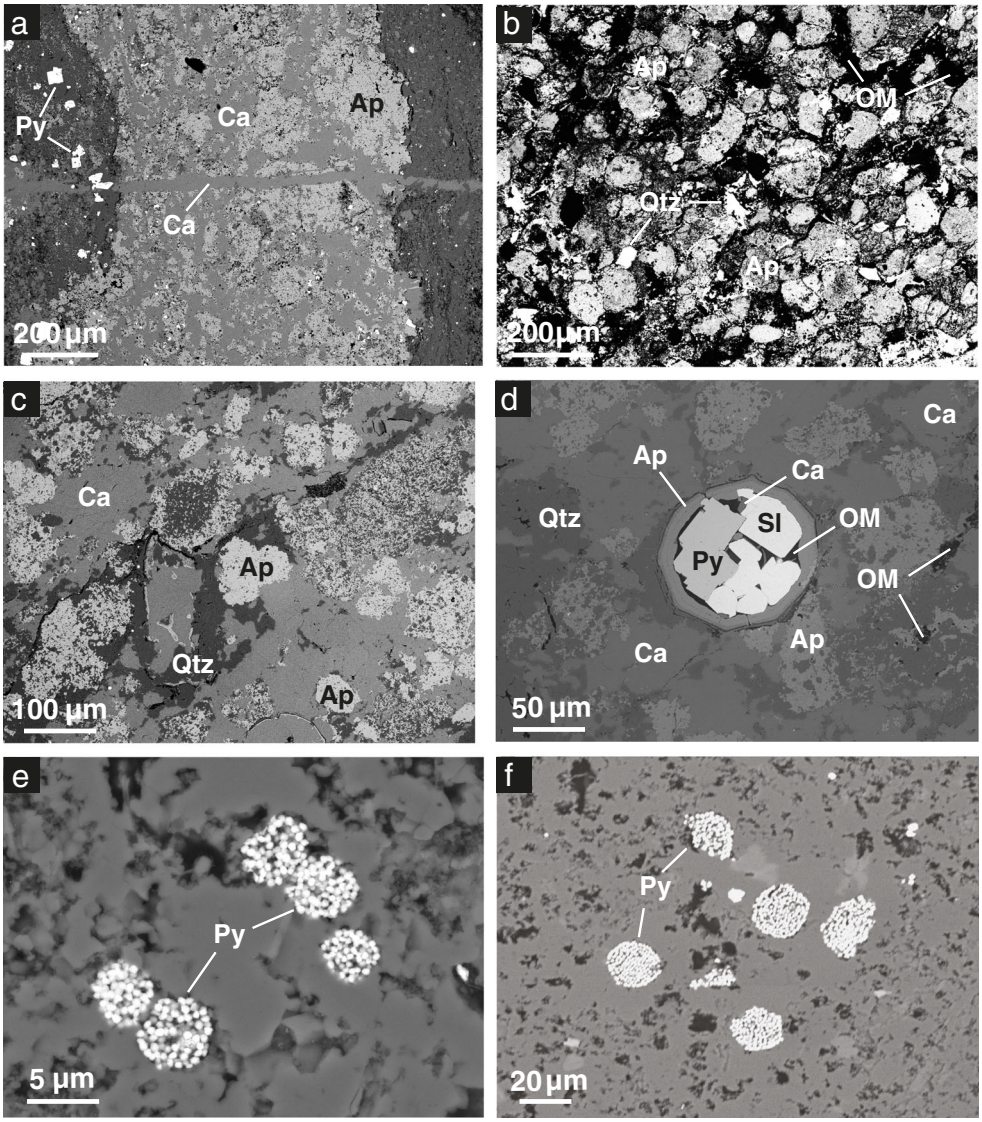

Fig. 6 Images of drill core samples. All are SEM-BSE (backscattered-electron) images unless noted. **a** Phosphatic lamina enclosed by organic-rich mudstone (*left* and *right*) from upper part of Upper siliceous mudstone member; note clastic grains of apatite in calcite matrix and late calcite veinlet; DDH XYC-116-225.0 m. **b** Photomicrograph of phosphorite from upper part of Upper cherty mudstone member, showing angular to rounded grains of apatite in a matrix of organic matter (*black*) and minor quartz (*white*); DDH XYC-216-157.1 m. **c** Clastic texture in phosphorite from uppermost part of Lower cherty member, showing angular grains of apatite and calcite in matrix of quartz and sparse organic matter (*black*); DDH XYC-145-98.0 m. **d** Round apatite peloid or phosphatic bioclast infilled by pyrite, sphalerite, and minor calcite and organic matter, surrounded by clastic matrix of apatite, calcite, and quartz, all within clastic-textured phosphorite; DDH XYC-145-98.0 m. **e** Pyrite framboids in organic-rich mudstone from upper part of Lower cherty member; DDH XYC-116-370.3 m. **f** Pyrite framboids in organic-rich mudstone from upper part of Active member; DDH XYC-116-326.8 m. Abbreviations: *Ap* apatite, *Ca* calcite, *OM* organic matter, *Qtz* quartz, *Py* pyrite, *Sl* sphalerite

calcite matrix (Fig. 6a); the apatite grains in some laminae are variably replaced by calcite.

Significantly, apatite concentrations are more widespread stratigraphically in the district than reported previously. The main horizons are in the lowermost part of the Active member and the uppermost part of the underlying Lower carbonaceous mudstone member. These intervals locally contain >18 wt% P_2O_5 and hence are true phosphorites (e.g., Trappe 1998), which have not been described in prior studies. Thicknesses of the phosphorites and other phosphate-rich beds range from several centimeters up to ~0.8 m. The predominant constituent is phosphate, accompanied by subordinate quartz, with lesser organic matter and calcite, plus sparse amounts of illite/smectite and pyrite. Most samples are deformed and contain sheared and variably recrystallized phosphate grains. Where early textures are preserved, individual phosphate grains vary from about 50 to

150 μm in diameter and display a clastic appearance within a matrix composed of varying proportions of organic matter, calcite, and quartz (Fig. 6b, c); rare coated grains have concentric growth zones developed along outer rims. A few phosphorites from the Active member contain appreciable sphalerite and galena, locally forming intergrowths with pyrite enveloped by a rim of laminated phosphate (Fig. 6d). The lower part of this member locally has laminae 0.5–1.5 cm thick composed of very fine-grained apatite intercalated with organic-rich mudstone that are very similar to occurrences in the Upper siliceous mudstone member.

Limestone

Beds 1 cm to as much as 2.5 m thick composed mainly of limestone occur throughout the lower part of the Duo Lake Formation but are volumetrically minor. The Active member contains siliceous limestone at and near the top and the base (Goodfellow and Jonasson 1986); this distinctive argillaceous limestone is used as a stratigraphic marker in the district. The underlying Lower cherty mudstone member contains thin limestone beds less than 0.5 m thick intercalated with black mudstone. Limestone beds also occur in the Pyritic mudstone member, but these appear to be uncommon.

Some intervals of limestone observed in drill core display graded bedding and cross-laminations that appear to be primary structures. All samples examined display fine-scale (<1 mm to 0.5 cm) layering and contain recrystallized calcite, minor organic matter, and sparse pyrite; limestone from the upper part of the Lower cherty mudstone member locally contains well-preserved radiolarians and sponge spicules (J.A. Dumoulin, written commun., 2013). Another sample of limestone from the top of the Active member has minor sphalerite and galena (2110 ppm Zn, 233 ppm Pb; DDH XYC-116-321.5 m).

Materials and methods

This study was designed to characterize in detail the bulk geochemistry of host rocks to the XYC deposit and evaluate the depositional conditions of these strata prior to, during, and after Zn-Pb mineralization. Drill cores were chosen with the goal of maximizing stratigraphic coverage and minimizing oxidation effects. Core XYC-116 was considered representative, although like most cores in this part of the district it does not penetrate the lower members of the Duo Lake Formation, below the Lower cherty mudstone member. Core H-42 studied by Goodfellow and Jonasson (1986), which intersected all members of the Duo Lake Formation, was not available for sampling. Core XYC-167 was selected to provide coverage of these lower strata, especially the Pyritic mudstone member. Locations of cores XYC-116 and XYC-167 are shown in Fig. 4. In total, 49 samples were analyzed from these two cores. A smaller number of samples (15) was collected from the Don deposit (Fig. 2; core DON-111), for comparison.

Samples used for bulk geochemistry were chosen so that only one lithology was represented. This strategy was achieved in most cases, except for several samples from the Upper siliceous mudstone member that contain interlaminated black mudstone and apatite, which were submitted as single samples, and hence yield mixed data for both lithologies. Also, intervals having visible sphalerite or galena were not analyzed, although microscopic and compositional data for these samples indicate that several contain minor amounts of these sulphides. Intervals containing visible pyrite were sampled, but not those having relatively thick (>1 cm) laminae.

Mineralogical studies were done at the U.S. Geological Survey in Reston, Virginia, using standard petrography (transmitted and reflected light), and scanning electron microscopy (SEM) for which two instruments were used. A JEOL JSM-840 SEM was operated at 15 kV and a beam current of 40 nA. This instrument has a LaB_6 electron emitter equipped with an EDAX energy-dispersive X-ray analytical system (EDS), which provides qualitative and semiquantitative elemental data. A Hitachi SU-5000 field-emission SEM was operated at 15 kV with a spot intensity of 30 at a working distance of 10 mm and used an EDAX Octane Plus Silicon Drift Detector EDS for compositional analysis.

Identification of fine-grained minerals was done by a PANalytical X'Pert Pro diffractometer, utilizing Cu Kα radiation to collect digital diffraction data continuously from 3° to 70° 2θ (scan speed = 0.0567° 2θ/s). PANalytical Highscore Plus software version 4.1 (2014) was used for pattern processing and semi-quantitative mineralogical analyses by Rietveld refinement, with an overall method reliability (determined from in-house prepared mixtures of comparable mineralogy) of ±1 % absolute (1σ) and minimum detection limit of 0.5 %.

Compositions of apatite were obtained by a JEOL JXA-8900R five-spectrometer, fully-automated electron microprobe at the U.S. Geological Survey in Denver, Colorado. Instrumental conditions were 15 kV, 20 nA beam current, and wavelength-dispersive X-ray spectrometry, using both natural and synthetic standards for major elements including Wilberforce (Ontario) apatite for F and Cl. Results for these halogens are constrained by variable crystallographic orientation and possible beam-induced migration during analysis (Stock et al. 2015).

Samples submitted for geochemical analysis consist of short intervals of split drill core ca. 5 to 8 cm in length, trimmed of weathered surfaces and veins, and pulverized in an alumina-ceramic mortar. All analyses were done at Activation Laboratories in Ancaster, Ontario. Major, selected trace, and rare earth elements (REE) were determined by ICP-MS on rock powders fused with lithium metaborate/tetraborate prior to analysis in order to insure complete acid dissolution of resistate minerals such as

zircon, monazite, xenotime, and barite. Instrumental neutron activation analysis (INAA) was used for As, Sb, Sc, and Cr. Concentrations of Li, B, Ga, Co, Cd, Au, Pb, Mo, Re, Te, and Se were acquired by high-resolution ICP-MS following a multi-acid digestion of powders. Total carbon and sulphur were determined by LECO infrared analyzer, CO_2 by coulometry after digestion with 2 N perchloric acid, total organic carbon (TOC) by difference after CO_2 removal and ignition to 600 °C, and SO_4 by difference after roasting to 850 °C; F was analyzed by specific ion electrode. Analyses were made on duplicate samples and on 8–12 standards. Precision and accuracy for concentrations ≥100 times the minimum detection limit (MDL) generally were better than ±5 % relative and in many cases, such as for major elements, were better than ±1 % relative. For concentrations approximately 10 times the MDL, precision and accuracy were about ±10–20 % relative, depending on the method used. Details of the various analytical methods are available online at www.actlabs.com.

Lithogeochemistry

Mudstone

Lithogeochemical data for selected components in cores XYC-116 and XYC-167 are shown in Fig. 7 and listed in Table 1 and Supplementary Data Table 1. Among 47 samples analyzed from these two cores, SiO_2 varies from 50.8 wt% to as much as 96.1 wt%, with the highest contents (>88 wt%) occurring in the upper part of the Active member and the lower part of the Upper siliceous mudstone member. MnO (not shown) is less than 0.05 wt% in all samples. TiO_2 does not exceed 0.8 wt%. Contents of P_2O_5 are uniformly low (<0.6 wt%) except in four intervals (1) the upper part of the Flaggy mudstone member where a few samples contain up to 2.7 wt% P_2O_5; (2) the Upper siliceous mudstone member, especially the upper part where seven samples over 13.3 m have 3.33 to 10.2 wt% P_2O_5; (3) locally in the lower part of the Active member where very high P_2O_5 contents (>18 wt%)

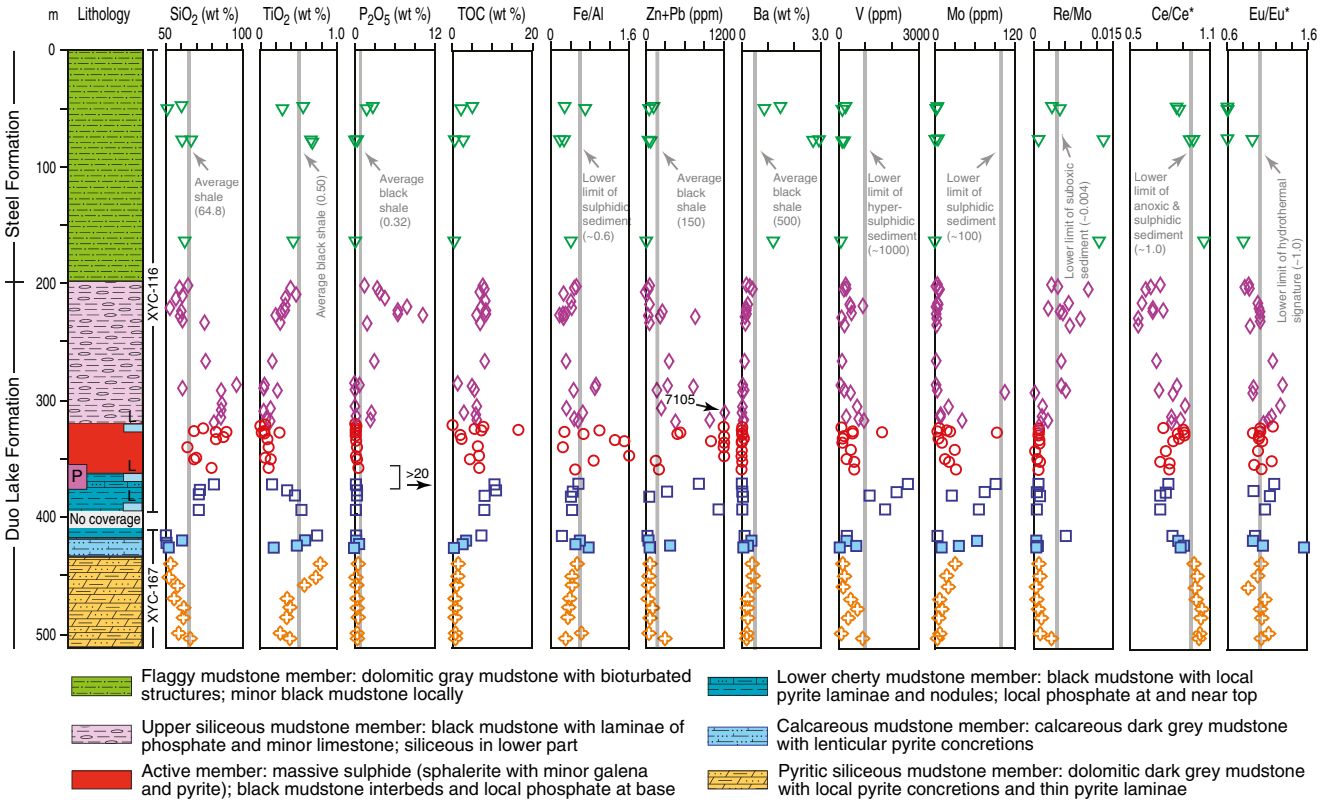

Fig. 7 Lithogeochemistry of XYC deposit. Upper part of section is from DDH XYC-116; lower part is from DDH XYC-167 (see text). All data are based on whole-rock analyses. Occurrences of >20 wt% P_2O_5 are in other drill holes (Fig. 1). Ce and Eu anomalies (Ce/Ce* and Eu/Eu*, respectively) are calculated using normalization to average post-Archean Australian shale (PAAS; Taylor and McLennan 1985); $Ce/Ce^*_{(SN)} = 2Ce_{SN}/(La_{SN} + Pr_{SN})$; $Eu/Eu^*_{(SN)} = 2Eu_{SN}/(Sm_{SN} + Gd_{SN})$, where SN represents shale normalization. Different colored symbols are linked to colors and lithologies of stratigraphic members shown on *left panel*. *L* limestone, *P* phosphorite. Sources of data for *vertical gray bars*: SiO_2 for average shale from Krauskopf and Bird (1995); TiO_2, P_2O_5, Zn + Pb, and Ba for average black shale from Ketris and Yudovich (2009); *Fe/Al* lower limit for sulphidic sediment from Lyons and Severmann (2006); *V* lower limit of hyper-sulphidic sediment from Scott et al. (2013); *Mo* lower limit of sulphidic sediment from Scott and Lyons (2012); *Re/Mo* lower limit of suboxic sediment from Ross and Bustin (2009); *Ce/Ce** lower limit of anoxic and sulphidic sediment from Slack et al. (2009); *Eu/Eu** lower limit of hydrothermal signature from Lottermoser (1992)

Table 1 Representative whole-rock analyses of mudstone from Howards Pass district

Sample	1	2	3	4	5	6	7	8	9	10
Unit	FLMD	USMS	USMS	USMS	ACTM	ACTM	ACTM	LCMS	CCMS	PSMS
SiO_2 (wt %)	60.87	60.08	61.11	85.80	74.31	68.35	69.78	81.35	51.87	57.66
Al_2O_3	13.73	4.10	4.82	1.26	1.48	5.08	1.37	2.96	9.66	12.02
$Fe_2O_3^T$	2.39	0.54	1.71	0.62	1.11	1.05	3.59	1.27	3.83	4.25
MnO	0.018	0.004	0.026	0.006	0.015	0.005	0.023	0.012	0.026	0.020
MgO	1.71	0.28	0.54	0.11	0.16	0.35	0.15	0.34	3.12	3.73
CaO	2.15	13.73	11.67	3.74	6.23	0.34	8.81	0.92	8.70	3.69
Na_2O	0.13	0.08	0.05	0.02	0.02	0.02	0.01	0.03	0.07	0.05
K_2O	5.36	1.87	1.79	0.48	0.45	1.89	0.50	1.05	4.22	5.78
P_2O_5	0.11	10.16	0.09	2.59	0.14	0.22	0.23	0.25	0.59	0.17
TiO_2	0.687	0.209	0.222	0.047	0.062	0.249	0.068	0.155	0.476	0.568
LOI	8.41	7.90	16.73	3.92	14.41	20.71	13.48	12.59	15.23	11.00
Total	95.57	98.95	98.76	98.60	98.39	98.27	98.02	100.90	97.81	98.94
F	0.06	0.86	0.20	0.24	<0.01	<0.01	<0.01	0.01	0.01	0.09
CO_2	3.25	0.05	8.96	0.34	4.85	0.35	7.33	0.47	10.7	6.72
TOC	3.01	6.29	5.50	2.94	7.88	16.48	4.35	10.5	2.54	1.34
Total S	1.04	0.32	1.31	0.57	0.72	0.82	2.73	0.53	1.39	1.79
SO_4	0.6	<0.3	<0.3	1.2	0.7	<0.3	1.4	<0.3	0.5	1.0
Li (ppm)	6.6	4.0	3.2	2.5	2.0	2.9	1.9	3.0	17.4	15.2
Be	3.0	2.0	3.0	0.5	0.8	1.7	0.8	2.0	1.2	1.0
B	29	39	15	16	14	35	9	13	39	23
Ga	19	7	6	2	3	9	2	5	13	16
Ge	2.6	2.5	1.9	1.0	4.2	7.7	4.9	3.0	1.4	<0.5
Sc	15.1	4.1	7.3	2.5	2.1	4.8	1.5	2.8	9.1	11.9
V	197	115	451	286	492	1626	283	2599	689	139
Cr	143	81	52	29	20	86	20	84	78	83
Nb	16.5	5.2	10.4	0.9	1.1	5.1	1.2	3.9	23.7	16.0
Ta	0.87	0.28	0.55	0.06	0.11	0.35	0.10	0.23	1.46	1.02
Zr	158	55	142	14	23	61	16	44	165	150
Hf	3.9	1.5	3.6	0.4	0.4	1.4	0.4	1.1	4.2	4.2
Th	10.2	4.84	4.88	1.93	1.70	5.58	1.24	2.78	11.9	12.4
U	4.40	13.5	17.1	13.4	7.70	47.4	5.53	98.7	29.1	11.8
Zn	31.0	24.7	4.6	7020	296	296	750	486	351	11.8
Pb	13.9	10.1	176	85.3	186	250	775	326	19.3	34.4
Cu	25.3	16.9	33.1	17.0	18.8	17.8	41.7	133	52.0	25.7
Co	9.3	3.2	9.0	1.6	3.1	9.8	3.9	5.9	12.4	18.7
Ni	57.4	74.6	57.8	28.1	42.9	121	81.1	152	98.9	70.6
Cd	0.02	0.07	<0.01	21.9	0.84	0.85	2.57	1.47	2.22	0.01
Ag	0.98	0.03	1.04	0.38	0.15	0.12	0.37	0.21	0.29	0.14
Au (ppb)	1.7	<0.5	0.5	<2	<2	<2	<2	<2	<2	13
As	19.5	3.7	18.4	4.3	11.7	17.8	38.8	13.0	28.2	30.5
Sb	2.08	0.22	4.47	0.97	1.01	2.08	4.27	5.05	3.57	4.34
Te	0.18	0.07	0.31	0.02	<0.02	0.09	0.09	0.21	0.03	<0.02
Se	2.3	2.4	3.2	1.6	0.9	1.6	1.9	2.7	3.9	1.2
Mo	0.98	0.90	105	6.06	17.2	92.8	15.4	91.1	35.6	19.9
Re	0.013	0.008	0.029	0.010	0.015	0.085	0.011	0.097	0.029	0.006
Sn	4	1	3	<1	<1	<1	<1	<1	<1	<1
W	2.0	2.3	<0.5	<0.5	0.5	1.4	0.7	2.4	1.2	0.5
Tl	0.58	0.52	0.12	0.61	0.19	2.51	0.30	0.69	0.33	1.51
Bi	0.3	0.1	0.1	0.1	0.1	0.1	0.1	0.1	0.2	0.2
Cs	0.67	0.51	0.20	0.23	0.16	0.43	0.16	0.34	1.64	2.10
Rb	20.7	20.9	7.8	8.6	5.9	12.7	4.9	10.1	37.1	29.0
Sr	36.3	109	57.7	27.7	28.3	5.8	37.8	13.0	115	43.9
Ba	28,550	1387	974	246	163	1011	154	125	2443	4496
Y	24.0	117	12.2	27.9	9.90	14.2	8.50	7.20	48.7	21.3
La	36.1	89.8	5.84	16.1	3.65	3.23	3.68	3.54	40.9	43.0
Ce	64.5	98.7	10.4	29.7	9.01	9.24	7.25	6.86	75.4	77.2
Pr	6.80	17.8	1.45	4.33	1.39	1.64	1.18	1.12	9.10	7.64
Nd	24.7	74.7	5.33	18.6	6.18	8.44	5.37	4.87	35.6	26.8
Sm	4.23	15.2	1.13	3.95	1.45	2.18	1.16	1.11	7.30	4.31
Eu	0.741	3.210	0.217	0.907	0.292	0.448	0.271	0.264	1.480	0.683
Gd	3.42	16.9	1.07	4.15	1.52	2.17	1.25	1.05	6.78	3.45
Tb	0.57	2.53	0.20	0.59	0.22	0.35	0.18	0.17	1.03	0.49
Dy	3.84	14.0	1.35	3.40	1.22	2.01	1.04	0.93	5.80	2.89
Ho	0.82	2.64	0.32	0.66	0.24	0.38	0.20	0.18	1.19	0.58

Table 1 (continued)

Sample	1	2	3	4	5	6	7	8	9	10
Unit	FLMD	USMS	USMS	USMS	ACTM	ACTM	ACTM	LCMS	CCMS	PSMS
Er	2.46	7.23	1.10	1.80	0.68	1.04	0.53	0.52	3.09	1.72
Tm	0.395	0.962	0.199	0.234	0.097	0.147	0.072	0.079	0.409	0.241
Yb	2.77	5.35	1.44	1.39	0.63	0.94	0.48	0.56	2.54	1.63
Lu	0.407	0.738	0.215	0.208	0.105	0.154	0.081	0.094	0.420	0.267
Ce/Ce^*_{SN}	0.945	0.568	0.824	0.818	0.895	0.859	0.792	0.785	0.902	0.974
Eu/Eu^*_{SN}	0.910	1.020	0.906	1.153	1.006	1.006	1.158	1.184	1.038	0.867

Note: Total iron as Fe_2O_3. Elements not detected and lower limits of detection (in parentheses): In <0.1 ppm; Ir <5 ppb. REE anomalies are calculated by shale normalization (SN) using data for PAAS (Taylor and McLennan 1985): $Ce/Ce^*_{SN} = 2Ce_{SN}/(La_{SN} + Pr_{SN})$; $Eu/Eu^*_{SN} = 2Eu_{SN}/(Sm_{SN} + Gd_{SN})$

Sample numbers: *1* XYC-116-76.0 m, *2* XYC-116-227.5 m, *3* XYC-116-290.0 m, *4* XYC-116-310.3 m, *5* XYC-116-323.8 m, *6* XYC-116-326.2 m, *7* XYC-116-349.4 m, *8* XYC-116-370.3 m, *9* XYC-167-285.5 m, *10* XYC-167-318.1 m

Abbreviations: *FLMD* Flaggy mudstone member, *USMS* Upper siliceous mudstone member, *ACTM* Active mudstone member, *LCMS* Lower cherty mudstone member, *CCMS* Calcareous mudstone member, *PSMS* Pyritic siliceous mudstone member

define phosphorites; and (4) commonly in the upper part of the Lower cherty mudstone member where similar very high P_2O_5 contents are observed.

Elevated to high TOC (~3 to 16.5 wt%) is characteristic of the Duo Lake Formation, except for the basal Pyritic siliceous mudstone member that has relatively low concentrations (<1.5 wt%). Fe/Al ratios are mostly less than 0.8 (lower limit for sulphidic sediment; Lyons and Severmann 2006), except for numerous samples from the Active member. Excluding the Active member, contents of Zn + Pb are greater than 600 ppm only in the Lower cherty mudstone member and the Upper siliceous mudstone member; one sample of siliceous and mildly phosphatic black shale from the latter member is highly anomalous in containing 7105 ppm Zn + Pb. Barium is low (<500 ppm) in all samples of the Duo Lake Formation, whereas gray mudstone in the overlying Flaggy mudstone member locally has 2.7 to 2.9 wt% Ba. Concentrations of V are below 1000 ppm except in one sample of black mudstone from the Active member (1626 ppm) and in four samples of black mudstone from the Lower cherty mudstone member (1157–2599 ppm); this same stratigraphic level in DON-111 has a similar range of high V contents (1206–2944 ppm; $n = 5$). The uppermost sample analyzed from the latter member (2599 ppm V) also has the highest U content (98.7 ppm), despite negligible P_2O_5 (0.25 wt%). The profile for Mo differs in that values above 30 ppm occur not only in the Active member and Lower cherty mudstone, but also in the Calcareous mudstone and Upper siliceous mudstone members. The maximum Mo content (105 ppm) is in the lower part of the Upper siliceous mudstone member. With one exception, samples having Re/Mo ratios above 0.04 are restricted to the Upper siliceous mudstone member and the Flaggy mudstone member. The highest $(Ge/Si) \times 10^6$ ratios of 0.19 and 0.24 (not shown) occur in black mudstone of the Active member; ratios for the other members are ≤0.15.

Overall abundances of REE are diverse among the different sampled units. Samples of gray dolomitic mudstone and black mudstone from the Flaggy mudstone member have abundances of ~0.4 to 1.5x PAAS, relatively flat patterns, and either small or no negative Eu anomalies (Fig. 8a). Black mudstone with varying amounts of apatite laminae from the Upper siliceous mudstone member (Fig. 8b) shows a large range of REE abundances (~0.01–3.0x PAAS), broadly flat patterns—some with relatively low ratios of light REE (LREE) to heavy REE (HREE). Values of Ce/Ce* and Eu/Eu* vary widely from 0.56 to 1.05 and 0.55 to 1.29, respectively. These values represent the magnitude of Ce and Eu anomalies, for REE data normalized to average post-Archean Australian shale (PAAS; Taylor and McLennan 1985). All Ce anomalies are genuine and not spurious based on a plot (not shown) of Pr/Pr* vs Ce/Ce* (cf. Bau and Dulski 1996). Ce/Ce* values are lowest (<0.7) in the upper part of the Upper siliceous mudstone member; Eu/Eu* values are highest (>1.0) in the Lower cherty mudstone member, the Active member, and the lower part of the Upper siliceous mudstone member. Samples of black mudstone and siliceous mudstone from the Active member (Fig. 8c) are distinctive in having uniformly low abundances (~0.04–0.5x PAAS) and especially depleted LREE with very low La/Sm ratios, regardless of the amounts of silica, carbonate, phosphate, TOC, or metals such as Zn and Pb. Data for black mudstone and calcareous mudstone from the underlying Lower cherty mudstone and Calcareous mudstone units (Fig. 8d) display a narrow range of abundances (~0.4–1.5x PAAS), flat patterns, small negative Ce anomalies, and no or small positive Eu anomalies. Samples of dolomitic and locally pyritic black mudstone from the Pyritic siliceous mudstone member (Fig. 8e) are similar to this overlying member in terms of abundance levels (~0.6 to 1.6x PAAS) and flat patterns but different in lacking Ce or Eu anomalies. Phosphorites from the Active and Lower cherty mudstone members (Fig. 8f) are distinguished by higher

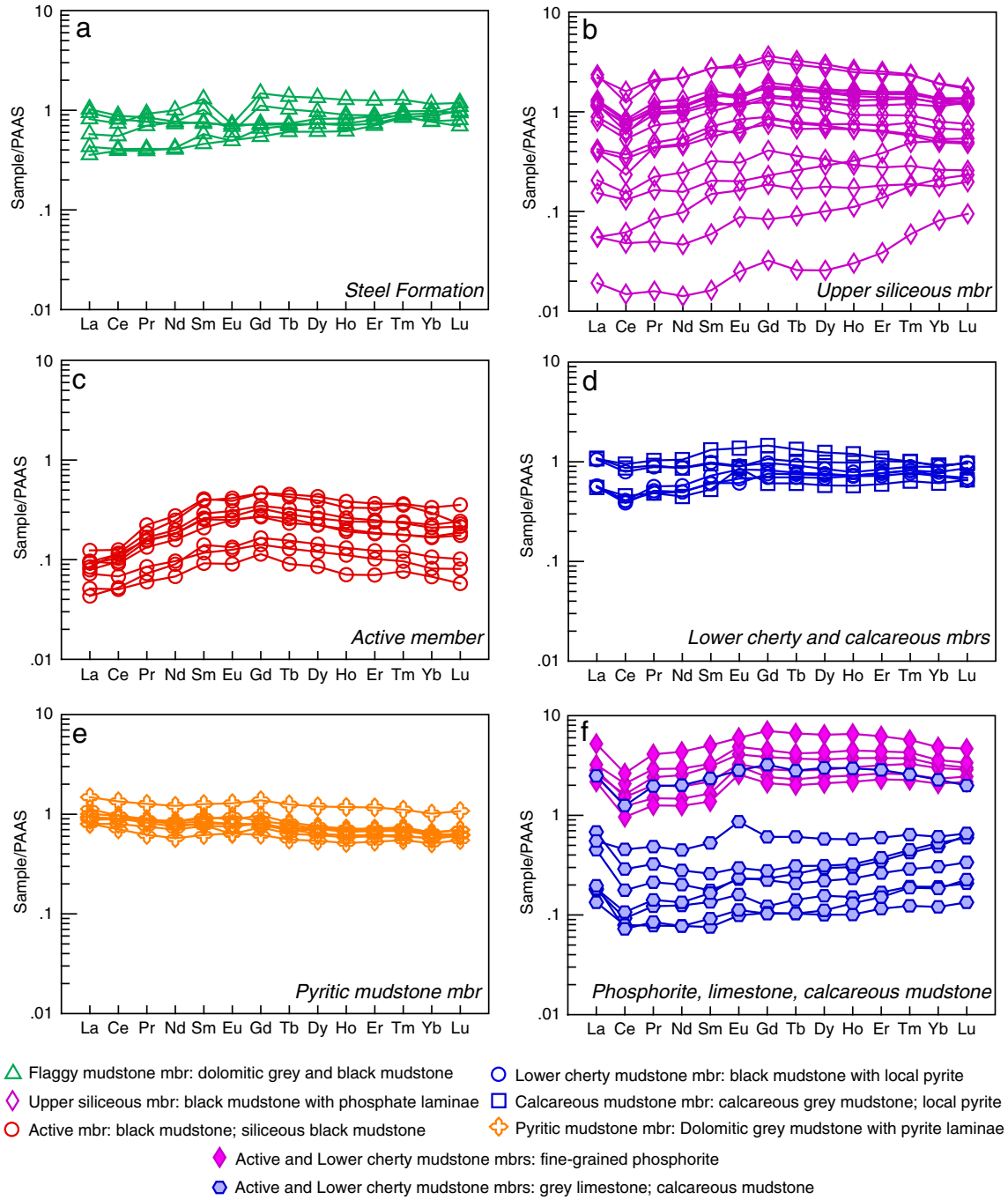

Fig. 8 Plots of REE concentrations normalized to PAAS (average post-Archean Australian shale) for black mudstone and other lithologies. Data show large ranges in abundances and presence (or absence) of Ce and Eu anomalies. **a** Flaggy mudstone member (Steel Formation). **b** Upper siliceous mudstone member. **c** Active member. **d** Lower cherty mudstone and Calcareous mudstone members. **e** Pyritic siliceous mudstone member. **f** Active and Lower cherty mudstone members: samples are phosphorite and limestone including one phosphatic limestone (highest abundances); some samples are from drill cores other than DDH XYC-116 or XYC-167. PAAS data from Taylor and McLennan (1985)

REE abundances (~1-7x PAAS), moderate negative Ce anomalies, and local small positive Eu anomalies. With the exception of one phosphatic sample, limestones differ in having relatively low abundances (~0.07–0.7x PAAS) and broad U-shaped patterns but are similar in terms of small negative Ce anomalies and no to small positive Eu anomalies.

A wide range of S/TOC ratios is apparent (Fig. 9a) in which limited S contents (<3 wt%) are present despite a large variation in TOC (<1 to 16.5 wt%; most <8.5 wt%). Some S/TOC ratios fall in the field for sulphate- and iron-limited sediments (Berner and Raiswell 1983), whereas others have variably higher S/TOC ratios. In terms of V contents (Fig. 9b), only five samples have

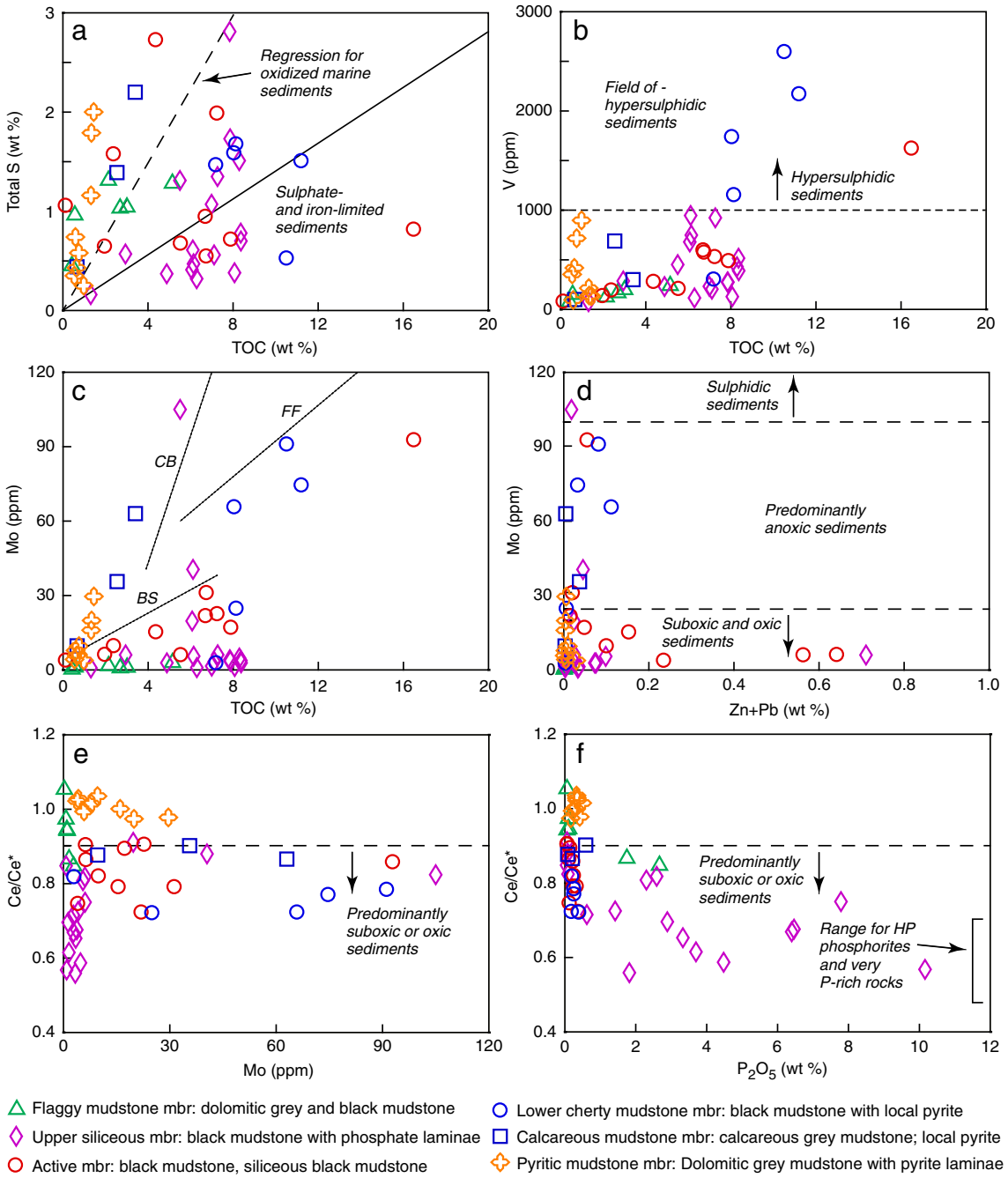

Fig. 9 Binary plots of bulk geochemical data for mudstone and other host rocks in DDH XYC-116 and XYC-167. Data show diverse redox signatures, including suboxic, anoxic, sulphidic, and hyper-sulphidic. **a** TOC vs S; field for sulphate- and iron-limited sediments, and regression line for normal oxidized marine sediments, from Berner and Raiswell (1983). **b** TOC vs V; field for hyper-sulphidic sediments from Scott et al. (2013). **c** TOC vs Mo; regression lines for organic-rich sediments of Cariaco Basin (*CB*), Framvaren Fjord (*FF*), and Black Sea (*BS*) from Algeo and Lyons (2006). **d** Zn + Pb vs Mo; fields for oxic to suboxic, predominantly anoxic, and sulphidic bottom waters based on data in Scott and Lyons (2012). **e** Mo vs Ce/Ce*; upper limit of field for predominantly suboxic and oxic sediments from Slack et al. (2015b) and references therein. **f** P_2O_5 vs Ce/Ce*; field for HP (Howard Pass) phosphorites and very P-rich rocks (15.9–24.7 wt% P_2O_5; $n = 8$) is based on analyses in Supplementary Data Table 1

more than the 1000 ppm cutoff for hyper-sulphidic sediments as defined by Scott et al. (2013). A plot of TOC vs Mo (Fig. 9c) shows only a small number of samples ($n = 6$) have sufficiently high Mo contents to plot near the regression lines for modern anoxic sediments from the Cariaco Basin and Framvaren Fjord; a few samples plot near the regression line for the Black Sea (see Algeo and Lyons 2006). No trends exist between contents of Zn + Pb and Mo (Fig. 9d); data for most samples plot in the fields for suboxic and oxic sediments or predominantly anoxic sediments. Values for Ce/Ce* (Fig. 9e) display a large range

Table 2 Representative whole-rock analyses of phosphorite from Howards Pass district

Sample	1	2	3	4	5	6
Unit	LCMS	LCMS	LCMS	LCMS	LCMS	ACTM
SiO_2 (wt %)	27.51	23.20	13.95	30.82	15.25	36.05
Al_2O_3	1.50	1.05	1.03	1.42	0.87	0.62
$Fe_2O_3^T$	2.48	2.01	2.29	1.24	1.14	0.39
MnO	0.009	0.013	0.015	0.011	0.019	0.009
MgO	0.20	0.13	0.12	0.18	0.12	0.08
CaO	33.82	37.43	42.18	33.58	45.45	30.44
Na_2O	0.04	0.03	0.04	0.03	0.04	0.03
K_2O	0.62	0.38	0.52	0.53	0.42	0.21
P_2O_5	22.99	23.66	24.73	21.69	24.47	18.67
TiO_2	0.045	0.043	0.046	0.035	0.037	0.018
LOI	8.92	10.49	11.81	9.19	10.19	8.33
Total	98.15	98.44	96.72	98.72	98.00	94.85
F	1.87	1.95	2.30	1.78	2.21	1.82
CO_2	2.44	4.57	5.80	3.12	8.49	2.35
TOC	4.33	4.31	4.13	4.52	2.02	4.41
Total S	1.95	1.60	2.21	0.84	0.94	1.21
SO_4	0.7	2.1	1.6	0.8	1.4	3.5
Li (ppm)	5.7	2.9	3.8	5.2	4.5	3.6
Be	2	2	2	2	2	2
B	27	34	32	41	53	55
Ga	3	3	2	4	2	3
Ge	1.2	1.0	<0.5	1.0	<0.5	<0.5
Sc	4.1	4.1	3.9	3.0	2.8	2.9
V	305	322	257	295	129	371
Cr	39	34	40	25	33	40
Nb	1.4	1.3	1.3	1.1	0.9	0.5
Ta	<0.01	<0.01	0.02	<0.01	0.03	<0.01
Zr	13	11	12	10	9	18
Hf	0.3	0.3	0.4	0.3	0.3	0.4
Th	0.95	0.71	0.93	0.74	0.72	1.84
U	69.5	20.2	41.3	81.3	43.4	151
Zn	3.1	10.9	8.9	179	1.8	8350
Pb	43.4	62.3	72.7	49.4	34.1	3260
Cu	15.4	19.9	19.4	9.50	12.3	65.5
Co	4.4	3.0	6.9	4.1	3.0	2.8
Ni	74.4	50.5	53.2	44.5	38.8	33.7
Cd	<0.01	0.07	0.03	0.84	<0.01	47.7
Ag	0.6	0.4	0.4	0.4	0.3	2.0
Au (ppb)	10	3	11	<2	<2	<2
As	51.4	33.7	48.9	21.7	19.1	18.2
Sb	10.5	5.86	9.30	5.13	3.65	20.1
Te	0.04	0.02	<0.02	<0.02	<0.02	<0.02
Se	4.2	3.3	2.4	3.3	2.2	6.7
Mo	15.9	13.7	7.33	6.69	2.22	21.7
Re	0.044	0.029	0.014	0.037	0.012	0.057
Sn	<1	<1	<1	<1	<1	<1
W	3.2	3.2	3.9	7.2	4.9	<0.5
Tl	0.14	<0.05	0.67	0.05	0.44	0.34
Bi	0.03	<0.02	<0.02	0.02	<0.02	0.12
Cs	0.40	0.30	0.29	0.43	0.26	0.19
Rb	16.4	12.0	12.2	16.1	10.8	7.5
Sr	293	304	410	250	393	230
Ba	180	165	215	103	190	230
Y	178	153	140	212	122	345
La	99.7	108	94.6	123	82.8	199
Ce	129	121	98.0	165	76.5	210
Pr	21.3	17.7	13.1	25.7	11.1	36.2
Nd	85.7	66.0	49.8	100	42.3	147
Sm	17.1	12.1	9.19	18.2	7.63	27.9
Eu	4.410	3.520	3.360	5.250	2.770	6.470
Gd	17.9	13.5	11.3	21.0	9.81	32.7
Tb	2.87	2.17	1.78	3.23	1.55	5.13
Dy	17.0	13.4	11.4	20.0	9.81	30.1
Ho	3.71	3.01	2.48	4.43	2.15	6.50

Table 2 (continued)

Sample	1	2	3	4	5	6
Unit	LCMS	LCMS	LCMS	LCMS	LCMS	ACTM
Er	10.7	9.03	7.50	12.5	6.54	17.7
Tm	1.510	1.330	1.040	1.730	0.916	2.310
Yb	9.10	8.40	6.57	10.1	5.86	13.6
Lu	1.300	1.240	1.060	1.460	0.940	2.020
Ce/Ce^*_{SN}	0.645	0.629	0.622	0.676	0.561	0.567
Eu/Eu^*_{SN}	1.242	1.366	1.665	1.360	1.621	1.078

Note: Total iron as Fe_2O_3. Elements not detected and lower limits of detection (in parentheses): In <0.1 ppm; Ir <5 ppb. REE anomalies are calculated by shale normalization (SN) using data for PAAS (Taylor and McLennan 1985): $Ce/Ce^*_{SN} = 2Ce_{SN}/(La_{SN} + Pr_{SN})$; $Eu/Eu^*_{SN} = 2Eu_{SN}/(Sm_{SN} + Gd_{SN})$

Sample numbers: *1* XYC-181-218.6 m, *2* XYC-181-219.4 m, *3* XYC-199-104.5 m, *4* XYC-203-370.5 m, *5* XYC-207-436.1 m, *6* XYC-216-157.1 m

Abbreviations: *LCMS* Lower cherty mudstone member, *ACTM* Active mudstone member

from 0.56 to 1.05, with the majority falling in the field of predominantly suboxic or oxic sediments (Slack et al. 2009 and references therein). A broad inverse trend exists between P_2O_5 and Ce/Ce* (Fig. 9f), in which samples having higher P_2O_5 contents display lower Ce/Ce* values, especially for the phosphorites and very P-rich rocks.

Limestone

Limited whole-rock geochemical data were acquired for seven samples of pale to dark gray limestone (Supplementary Data Table 1). Bulk compositions are variable in terms of SiO_2 (2.08–44.0 wt%) but relatively uniform in MgO (0.09–0.56 wt%), TOC (0.96–2.41 wt%), and total S (0.09–1.05 wt%). MnO is negligible (<0.08 wt%). Contents of P_2O_5 are very low (<0.16 wt%) except in one phosphatic limestone from the uppermost part of the Lower cherty mudstone member (XYC-145-98.0 m) that has 9.08 wt%. This P-rich sample also is geochemically anomalous, relative to the other limestones, in having elevated Zn (1070 ppm), Pb (75 ppm), Cu (83 ppm), and U (46.9 ppm).

REE data (Fig. 8f) show abundances of ~0.07 to 8x PAAS, excluding the one phosphatic limestone. All analyzed samples display small negative Ce anomalies. Significantly, positive Eu anomalies are characteristic, ranging from 1.07 to 1.56, the largest value occurring in a limestone at the top of the Active member that also contains elevated Zn and Pb (2100 and 233 ppm, respectively).

Phosphate-rich strata

Whole-rock analyses of six phosphorite samples from the Active and Lower cherty mudstone members (Table 2) show 18.7 to 24.7 wt% P_2O_5 and high silica contents of 14.0 to 36.1 wt% SiO_2. Concentrations of other major oxides are uniformly low; Fe/P ratios range from 0.03 to 0.17 and average 0.11 ± 0.05. TOC and F vary from 2.02 to 4.52 wt% and 1.78 to 2.30 wt%, respectively. All but two analyzed samples lack elevated base metals (<250 ppm Zn + Pb + Cu). One exception, from near the base of the Active member, is a chalcopyrite-bearing interval (921 ppm Cu) in DON-189 at 299.7 m. The second is from the lower part of the Active member and contains abundant sphalerite and galena (1.16 wt% Zn + Pb) in XYC-216 at 157.1 m; a comparable stratigraphic level in XYC-302 at 521.5 m also has appreciable Zn + Pb (7180 ppm) but is not a phosphorite sensu stricto (7.62 wt% P_2O_5). Contents of other trace elements and REE are generally low in the phosphorites, except in XYC-216-157.1 that has 151 ppm U and elevated light REE (e.g., 199 ppm La). A shale-normalized plot (Fig. 8f) shows abundance levels of ~1.0 to 7x PAAS and a relatively narrow range of La/Yb ratios from 11.0 to 14.6. All six samples display moderate negative Ce anomalies (Ce/Ce* 0.56–0.68) and small positive Eu anomalies (Eu/Eu* 1.08–1.67).

Apatite grains from the Lower cherty, Upper siliceous mudstone, and Flaggy mudstone members were analyzed for major elements, halogens, and LREE by electron microprobe (EMP) methods (Table 3). Reconnaissance data (n = 35) obtained for four samples show that some apatite in the Lower cherty member has higher Cl contents relative to that in the Upper siliceous mudstone member and overlying Flaggy mudstone member of the Steel Formation and in the Active member based on data from Gadd et al. (2016a) (Fig. 10). Concentrations of Y, LREE, and U are very low or below detection limits in all analyses. Previous workers (e.g., Goodfellow and Jonasson 1986; Goodfellow 2007) used the term francolite or carbonate fluorapatite for these apatite occurrences in the Howards Pass district. This classification requires the presence of excess F (>2.00 apfu) in the M2 site in order to provide sufficient charge balance for the substitution of CO_3^{2-} for PO_4^{3-} in the tetrahedral site (see McClellan and Van Kauwenbergh 1990). However, approximately 30 % of our EMP analyses lack excess F and hence are fluorapatite (with minor CO_3); the remaining analyses have F > 2.00 apfu and thus are designated as francolite. Gadd et al. (2016a) reached the conclusion that apatite in the district spans

Table 3 Representative electron microprobe analyses of apatite from Howards Pass district

Sample	1	2	3	4	5	6	7
Unit	FLMD	USMS	USMS	LCMS	LCMS	LCMS	LCMS
CaO (wt %)	56.29	54.80	56.50	53.44	54.53	54.60	54.69
Na_2O	0.04	0.05	0.05	0.31	0.21	0.17	0.11
MnO	0.00	0.00	0.00	0.00	0.00	0.00	0.00
FeO	0.11	0.00	0.00	0.08	0.06	0.04	0.04
Y_2O_3	0.07	0.08	0.02	0.05	0.13	0.18	0.16
La_2O_3	0.00	0.00	0.00	0.00	0.00	0.09	0.00
Ce_2O_3	0.00	0.10	0.10	0.00	0.00	0.00	0.00
Pr_2O_3	0.00	0.00	0.00	0.00	0.00	0.00	0.00
Nd_2O_3	0.06	0.03	0.00	0.00	0.04	0.05	0.05
P_2O_5	39.70	40.45	40.97	41.54	41.44	41.12	40.99
SiO_2	0.00	0.00	0.00	0.00	0.00	0.00	0.00
SO_3	0.26	0.07	0.07	0.12	0.10	0.08	0.05
Cl	0.01	0.02	0.01	0.15	0.11	0.06	0.04
F	3.79	3.81	3.82	4.03	2.92	3.76	3.83
Total	100.32	99.41	101.54	99.72	99.52	100.16	99.96
Cations on the basis of 26 oxygens							
C (apfu)	0.218	0.092	0.128	0.000	0.000	0.050	0.058
Ca	10.39	10.13	10.25	9.772	10.03	9.997	10.03
Na	0.013	0.018	0.015	0.104	0.071	0.057	0.036
Mn	0.000	0.000	0.000	0.000	0.000	0.000	0.000
Fe	0.016	0.000	0.000	0.012	0.009	0.006	0.005
Y	0.006	0.007	0.002	0.004	0.012	0.016	0.014
La	0.000	0.000	0.000	0.000	0.000	0.005	0.000
Ce	0.000	0.006	0.006	0.000	0.000	0.000	0.000
Pr	0.000	0.000	0.000	0.000	0.000	0.000	0.000
Nd	0.004	0.002	0.000	0.000	0.002	0.003	0.003
P	5.782	5.908	5.872	6.001	6.024	5.950	5.942
Si	0.000	0.000	0.000	0.000	0.000	0.000	0.000
S	0.034	0.009	0.009	0.015	0.012	0.010	0.007
Cl	0.002	0.006	0.004	0.044	0.031	0.018	0.013
F	2.062	2.078	2.044	2.176	1.583	2.034	2.072

Notes: Total iron as FeO; C calculated by difference. Analyzed but below detection limit of ~0.01 wt %: Al_2O_3, Eu_2O_3, Sm_2O_3, Gd_2O_3, Dy_2O_3, Er_2O_3, ThO_2, UO_2, PbO

Sample numbers: *1* XYC-116-46.8, *2* XYC-116-212.5 m, *3* XYC-116-225.0 m, *4* XYC-116-376.5 m, *5* XYC-116-376.5 m, *6* XYC-116-376.5 m, *7* XYC-116-376.5 m

Abbreviations: *FLMD* Flaggy mudstone member, *USMS* Upper siliceous mudstone member, *LCMS* Lower cherty mudstone member

a compositional range from carbonate-bearing fluorapatite to francolite.

Discussion

Episodic Zn-Pb mineralization

Early exploration work and recent studies have demonstrated that Zn-Pb zones in the Howards Pass district are not restricted to the Active member. These other occurrences are relatively rare, however. Laminated sphalerite and galena exist in the middle part of the Upper siliceous mudstone member (up to 7.0 wt% Zn over 0.5 m in XYC deposit) and in the lower part of the Backside siliceous mudstone member (Portrait Lake Formation) overlying the Flaggy mudstone member (Goodfellow and Jonasson 1986; Gadd et al. 2016b). Moreover, our whole-rock geochemical data for drill core XYC-116 document locally high Zn and/or Pb contents in the lower part of the Upper siliceous mudstone member, reaching grades up to 7020 ppm Zn or 448 ppm Pb (Supplementary Data Table 1). Elevated Zn (1040 ppm) is

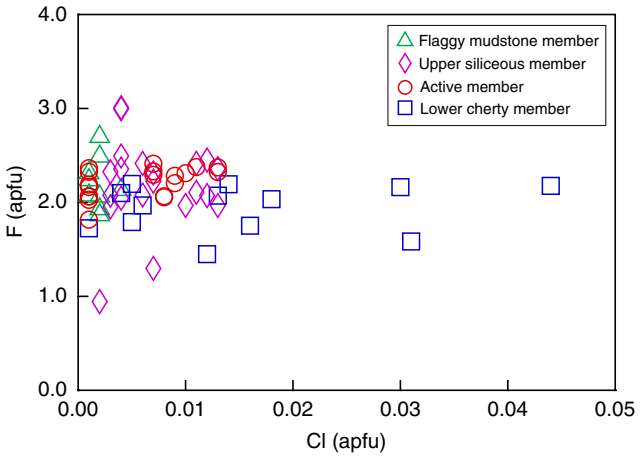

Fig. 10 Plot of Cl vs F contents of apatite from Flaggy mudstone member (46.8 m), Upper siliceous mudstone member (212.5 and 225.0 m), and Lower cherty member (376.5 m) in DDH XYC-116. Also shown are data from Gadd et al. (2016a) for apatite in Upper siliceous mudstone and Active members in DDH XYC-190 and XYC-224. Data show high Cl contents in some samples from Lower cherty member. All results by electron microprobe analysis. Abbreviation: *apfu* atoms per formula unit

also present locally in the Lower cherty mudstone member, well below the base of the Active member. Additional evidence for hydrothermal effects below and above the Active member derives from (1) elevated (Ge/Si) × 10^6 ratios of 0.12 to 0.15 in three samples of the Upper siliceous mudstone member (ratios are up to 0.24 in the Active member), and the related interpretation that in most settings high Ge/Si ratios are fingerprints of hydrothermal activity (Mortlock et al. 1993; Slack et al. 2004b); and (2) Eu/Eu* values above 1.1, especially in the upper part of the Lower cherty mudstone member and the lower part of the Upper siliceous mudstone member, such positive Eu anomalies being hallmarks of hydrothermal fluids (Lottermoser 1992; Slack et al. 2004b). A possible link of these Eu anomalies to reduced alkaline pore fluids (Sverjensky 1984) may be valid for samples of limestone and calcareous mudstone that mostly have small positive Eu anomalies (Fig. 8f) and lack elevated Zn + Pb (Supplementary Data Table 1), but is considered unlikely for the non-calcareous mudstone samples based on a lack of correlation (not shown) between Eu/Eu* and Mo contents (see Slack et al. 2015c and references therein). Collectively, these results suggest that hydrothermal processes affected strata well below and above the Active member, including as much as 200 m (or more) above the Zn-Pb deposits. If these stratigraphically widespread occurrences of sphalerite and galena in the district are not of late diagenetic or tectonic origin (see Gadd et al. 2016b), then they may record episodic Zn-Pb mineralization linked to multiple syngenetic-exhalative and/or early diagenetic hydrothermal events.

A replacement model for the Howards Pass Zn-Pb deposits should also be considered. Most workers have proposed an origin involving syngenetic precipitation of sulphides (sphalerite, galena, pyrite) from a hydrothermal brine pool (Goodfellow and Jonasson 1986; Goodfellow 2007; Ootes et al. 2013). Recently, Gadd et al. (2016b) invoked a modified exhalative model involving the downward percolation of dense metalliferous brines into unconsolidated sediments (see Sangster 2002). A third possibility is that the Zn-Pb deposits formed by the selective replacement of limestone or other reactive strata. Occurrences of graded beds and cross-laminations in limestones from the Active member and underlying Lower cherty mudstone member, as described above, are consistent with deposition as distal carbonate turbidites (e.g., Lowe 1982). The presence of minor pyrite and local sphalerite within these limestones, and the replacement of sponge spicules, radiolarians, and other fossils by pyrite and sphalerite (Jonasson and Goodfellow 1986; Kelley et al. 2016), as well as moderate positive Eu anomalies up to 1.56 (Fig. 8f), suggest that some Zn-Pb deposits in the Howards Pass district may have formed by this mechanism. However, if these deposits formed mainly by replacement, it likely occurred during or shortly after burial and compaction of the sediments and not tens to hundreds of millions of years later, based on recent Re-Os dating of early pyrite in the deposits (Kelley et al. 2016). In summary, the weight of available evidence (Jonasson and Goodfellow 1986; Goodfellow 2007; Gadd et al. 2016b, c) suggests that the Howards Pass Zn-Pb deposits formed mainly by syngenetic and early diagenetic processes, the latter including the downward percolation of dense metalliferous brines into unconsolidated sediments, and local replacement of carbonate during and shortly after sedimentation.

Redox states of bottom waters and pore fluids

Evaluating the redox state of bottom waters and pore fluids in ancient sedimentary rocks is challenging due to effects of varying depositional settings, to diagenesis and metamorphism, and to the typically conflicting signals recorded by different geochemical proxies (e.g., Algeo and Rowe 2012). Additional complications include the possibility of diverse redox conditions in bottom waters and contemporaneous pore fluids, as in some modern settings where oxic bottom waters overlie organic-rich sediments that contain anoxic or sulphidic pore fluids (e.g., Canfield et al. 1993). A final caveat relates to geologically rapid changes in redox state that may be represented in only a few centimeters of sediment—owing to environmental changes over tens of thousands of years or less—which can be missed by the analysis of single samples that cover a larger stratigraphic (and age) range. In this report, we use several mineralogical and geochemical proxies that in some cases provide conflicting redox states, a situation also reported in other studies. However, with few exceptions, there

is strong evidence for a predominant redox state within each stratigraphic unit, as described below.

Geochemical proxies suggest that rocks of the Duo Lake Formation in the Howards Pass district were deposited under varying redox conditions (Figs. 7 and 9). At the base, the Pyritic siliceous mudstone member has relatively low Fe/Al ratios and low Mo and V contents that collectively argue against sulphidic bottom waters, although anoxic conditions are likely—especially in the upper parts of the member—based on sulphur isotopes and degree of pyritization (DOP) for this unit (Goodfellow and Jonasson 1986; Johnson et al. 2014). Deposition of this member is attributed to a discrete basin, which likely was marginal and external to the shelf (Goodfellow 2007), although a shelf-hosted internal basin cannot be ruled out. Gradual restriction of this basin is inferred based on coupled stratigraphic trends for $\delta^{34}S$ values and Mo/TOC ratios (Johnson et al. 2014).

Geochemical and isotopic data for the overlying Calcareous mudstone member are broadly similar, thus also implying anoxic bottom waters. Samples from the middle and upper part of the Lower cherty mudstone member differ in having higher contents of V and Mo (with one exception); these results suggest anoxic to intermittently sulphidic conditions (Tribovillard et al. 2006; Scott and Lyons 2012), including possible hyper-sulphidic conditions for samples having over 1000 ppm V (Breit and Wanty 1991; Scott et al. 2013). Sulphidic bottom waters in the upper part of the Lower cherty mudstone member are supported by the generally small size (4–6 μm) of rare pyrite framboids (Fig. 6e), which suggests precipitation of Fe-sulphide precursor(s) in the water column based on studies of the size range of pyrite framboids in modern sediments including those of the Black Sea (Wilkin et al. 1997). However, it should be noted that framboidal pyrite is uncommon in unmineralized black mudstone below the Active member, in contrast to widespread occurrences of small dispersed grains of euhedral pyrite that likely formed by the diagenetic (or tectonic) recrystallization of framboids and by precipitation from hydrothermal fluids (see Gadd et al. 2016b).

The redox state of bottom waters during deposition of the Active member may have ranged widely from suboxic to sulphidic. Fully oxic conditions are unlikely based on very low MnO contents in all samples of black mudstones analyzed (≤0.03 wt%; $n = 9$). Suboxic conditions are implied by mostly low Mo concentrations of less than 25 ppm (Figs. 7 and 9) that indicate H_2S was restricted to pore fluids (Scott and Lyons 2012), in concert with relatively low Ce/Ce* values of 0.72 to 0.91 although these values may, at least in part, reflect detrital phosphate and hence not be an accurate redox proxy for local bottom waters (compare Fig. 9d, e). Pyrite framboids within the Active member show a large size range from 3 to 25 μm (Fig. 6f), attributed by Gadd et al. (2016b) to predominantly suboxic conditions (see also Wignall and Newton 1998). In contrast, Re/Mo ratios are very low (<0.002) and suggest anoxic to sulphidic depositional conditions, based on studies by Ross and Bustin (2009); their Re/Mo discrimination plots may not be sensitive at low Mo concentrations; consequently, we rely on the more recent perspective of Scott and Lyons (2012) that implies predominantly suboxic bottom waters. However, in the middle part of the Active member, one sample of black mudstone (low Zn + Pb) has 92.8 ppm Mo, which is consistent with a geologically brief period of anoxic to sulphidic conditions, assuming minimal influence by a high sedimentation rate, pH variation, or low aqueous Mo in the water column (see Scott and Lyons 2012). An additional uncertainty is whether thermal maturity during diagenesis affected the Mo contents (Ardakani et al. 2016), although this seems unlikely given the relatively large range observed; hydrothermal mobilization of Mo cannot be ruled out, but the lack of correlation between Mo and Zn + Pb (Fig. 9d) argues against addition of Mo by the metalliferous hydrothermal fluids. The prominent spikes in Fe/Al ratios within parts of the Active member (Fig. 7) likely record the hydrothermal deposition of pyrite (Johnson et al. 2014). High SiO_2 contents (~83–90 wt%) are independent of redox state and are interpreted to mainly reflect the addition of biogenic silica derived mainly from radiolarians.

During deposition of the Upper siliceous mudstone member, the early bottom waters appear to have fluctuated from suboxic to sulphidic conditions and later shifted to uniformly suboxic conditions. This interpretation is based collectively on signals derived from Mo contents, Mo/Al ratios, Re/Mo ratios, and Ce/Ce* values. Specifically, mudstone samples from the lower part of this member have 5.5 to 40.5 ppm Mo, and Re/Mo ratios of 1.4 to 2.7×10^{-3}, both of which imply suboxic or anoxic bottom waters. However, the next higher sample, 14.8 m stratigraphically above, has 105 ppm Mo and a Re/Mo ratio of 0.3×10^{-3} that together provides strong evidence of sulphidic bottom waters. In contrast, samples from the upper part of this member—mostly phosphatic black mudstone—have uniformly low Mo contents (<6.2 ppm) and relatively high Re/Mo ratios ($2.8–10.4 \times 10^{-3}$); Ce/Ce* values are systematically low (0.56–0.85), reflecting moderate to small negative Ce anomalies.

The flaggy mudstone member of the Steel Formation was likely deposited under suboxic conditions based on textures and compositions. This member is distinct in the district in containing widespread bioturbation features that indicate at least minor oxygenation of bottom waters and pore fluids (e.g., Wignall 1994). Based on a limited database ($n = 6$), fully oxic conditions are ruled out by low MnO contents (≤0.04 wt%). Predominant suboxic conditions are supported by very low Mo (<3.0 ppm) and high Re/Mo ratios ($3.5–13.3 \times 10^{-3}$) excluding data for one sample. This redox assignment is supported by Ce/Ce* values, which are mostly less than 0.95 and thus define small negative Ce anomalies.

Apatite dissolution and Zn-Pb mineralization

The distinctive REE pattern of black mudstones from the Active member (Fig. 8c) has implications for the origin and timing of Zn-Pb mineralization in the district. The low abundances of LREE (La to Nd) within this member, relative to other REE, contrast with those of all other members of the Duo Lake and Steel formations, thus indicating that the loss of LREE is not related to normal diagenesis of the local sedimentary sequence. Nor is it likely to be a function of sedimentary sorting or an unusual source terrane (e.g., McLennan 1989), given the broadly similar major and trace-element compositions of the mudstone samples from the Active member and those from the other members. Conceivably, the low LREE abundances and P_2O_5 contents (0.06–0.37 wt%) of Active member mudstones could reflect the loss of accessory apatite or monazite, both of which are characterized by greatly enriched LREE relative to HREE. Apatite is much more soluble in low-temperature fluids than is monazite (Ayers and Watson 1991); hence, the unusual REE pattern of these mudstones likely records the preferential loss of sedimentary apatite. This interpretation is based on the role of accessory apatite in controlling the flat (i.e., non-LREE depleted) PAAS-normalized REE patterns that characterize Paleozoic shales worldwide (McLennan 1989) and on the assumption that apatite was present as an accessory mineral in mudstones of the Active member prior to Zn-Pb mineralization. Leaching of apatite probably occurred during diagenesis, when pore fluids were present. Apatite dissolution (fluorapatite and carbonate fluorapatite) is not influenced by elevated temperature owing to effects of retrograde solubility, nor to changes in pressure, X_{H2O}, or M_{NaCl} (Atlas and Pytkowicz 1977; Ayers and Watson 1991). However, acidic fluids can readily dissolve apatite, even at low temperature, but above a pH of ~6.5 (at 25 °C) this mineral is only sparingly soluble (Chaïrat et al. 2007). Assuming that sediment pore fluids in the Active member were predominantly anoxic—based on redox proxies such as Mo described above—the pH of these pore fluids was likely ca. 6.6, due to self-buffering related to H_2S-carbonate equilibria as observed in modern anoxic pore fluids (Burdige 2006). Therefore, reactions in normal marine pore fluids probably did not cause the pervasive dissolution of apatite in mudstones of the Active member.

The presence of abundant sphalerite and galena in the Active member suggests a genetic link between Zn-Pb mineralization and dissolution of apatite in this member. Although the acidity of fluids responsible for deposition of ancient CD Pb Zn deposits is unknown, modern metalliferous sedimentary brines that contain elevated Zn and Pb have pH values of ~3.5 to 6.0 (Hanor 1996). These variably acidic fluids, if not greatly diluted by overlying seawater, would be expected to readily dissolve apatite, both fluorapatite and carbonate fluorapatite, even at an ambient temperature of 25 °C. An alternative explanation involving restricted apatite precipitation in highly alkaline pore fluids is considered unlikely because accessory carbonate minerals are widespread in underlying and overlying members that lack the anomalously low LREE abundances of the Active member (Fig. 8). On balance, therefore, we propose that the distinctive LREE-depleted patterns for black mudstones of the Active member preferentially record the passage of Zn- and Pb-bearing metalliferous fluids. Significantly, this hypothesis has implications for the mechanism of Zn-Pb deposition. The classic exhalative model of seafloor

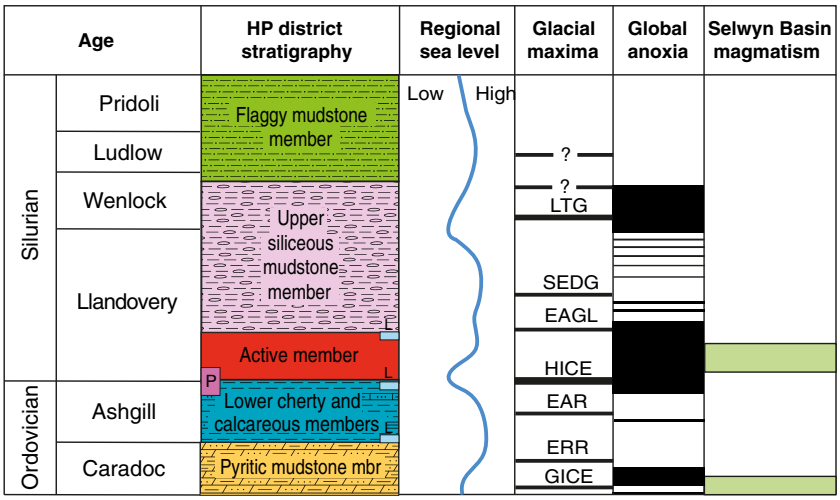

Fig. 11 Environmental events and changes during Ordovician and Silurian time applied to Howards Pass district. Regional sea level (for central Mackenzie Mountains, NWT) from Lenz (1982); glacial maxima (global) from Page et al. (2007) and Calner (2008); global anoxia from Page et al. (2007); Selwyn Basin magmatism from Goodfellow et al. (1995) and Goodfellow (2007). *L* limestone, *P* phosphorite. Abbreviations for glacial maxima: *LTG* late Telychian glaciation, *SEDG* Sedgwickii zone glaciation, *EAGL* early Aeronian glaciation, *HICE* Hirnantian glaciation, *EAR* early Ashgill regression, *ERR* early Rakvere regression, *GICE* Guttenberg regression. Trends suggest that phosphorites were deposited during or shortly after the HICE glaciation and that Zn-Pb sulphides were deposited during a major global anoxic event coeval with mafic magmatism elsewhere in Selwyn Basin (see text for discussion)

precipitation of sphalerite and galena (and pyrite) from a metalliferous brine is herein considered unlikely, because it does not explain the leaching of apatite from samples of black mudstone that have negligible Zn or Pb contents (149–546 ppm Zn + Pb in four samples), as well as appreciable variations in SiO_2, Al_2O_3, TOC, and Mo (see Supplementary Data Table 1). However, the modified model of Sangster (2002) involving the downward percolation of dense metalliferous brine would likely include the dissolution of apatite, assuming that a mildly acidic pH was maintained in the brine on the seafloor and during the percolation process, without a shift to circumneutral pH due to dilution by seawater or pore fluids. This model also explains intervals in the Active member of unmineralized—but LREE-depleted—black mudstone up to 10 cm thick that alternate with layers of high-grade sphalerite ± galena (± pyrite), via the selective deposition of these sulphides where sufficient H_2S was available, either preexisting in pore fluids or derived from an external source. A different scenario in which metalliferous brines migrate upward is not favored because such brines would likely be channeled in fractures and faults and hence not be distributed throughout the mudstone strata that host the Zn-Pb deposits. Similarly, a wholly replacement model involving the diagenetic introduction, chiefly parallel to bedding, of an acidic hydrothermal fluid would also dissolve apatite (and carbonate) but would do so mainly within permeable beds, given the likelihood during diagenesis of partial lithification of the sediment and a low permeability related to the presence of abundant clays. In summary, we prefer a model in which the distinctive LREE-depleted patterns of unmineralized black mudstone in the Active member are intimately linked to Zn-Pb mineralization, including the deposition of sulphides involving the downward percolation of a dense metalliferous brine. This model is also consistent with the presence of K-feldspar within the Upper cherty mudstone member that suggests an origin involving acidic hydrothermal fluids (Goodfellow 1984).

Glaciation and sea-level changes

The Ordovician and Silurian periods are noteworthy for recording major environmental changes (Fig. 11). Key events that occurred globally during the Late Ordovician include a major rise in sea level and the subsequent Hirnantian glaciation (Ghienne et al. 2014). These events are relevant for Zn-Pb and phosphate mineralization in the Howards Pass district based on the likelihood that organic-rich sediments, such as those in the Duo Lake Formation, preferentially accumulate during transgression linked to global icehouse conditions (e.g., Page et al. 2007). Based on data from the central Mackenzie Mountains (Lenz 1982), sea level rose following the Hirnantian glaciation, contemporaneously with deposition of the Active member. During deposition of this member, within the Rhuddanian (lower Llandovery) based on conodonts (Norford and Orchard 1985), global sea level continued to rise due to melting of Gondwanan ice sheets (Loydell 1998) and remained high during deposition of the lower and middle parts of the Upper siliceous mudstone member (cf. Munnecke et al. 2010).

Intervals in the Duo Lake Formation that contain the highest TOC contents occur in the upper part of the Lower cherty member and the upper part of the Active member (11.2 and 16.5 wt%, respectively). The former stratigraphic level corresponds approximately to the highest concentrations of P_2O_5, present in phosphorite (Fig. 7), and may represent a maximum flooding surface (see Creaney and Passey 1993). The latter is one of two levels in the Active member—lower and upper—that contain high Zn + Pb grades (Kirkham et al. 2012). Compared to the lower-grade zones occurring in the middle part of the Active member, Zn-Pb-Fe sulphides in the high-grade zones are much coarser grained and typically display sheared and mylonitic textures, likely reflecting deformation-related recrystallization and thrust faulting (Fig. 3; Jonasson and Goodfellow 1986; Hodder et al. 2014). However, it is unclear if these two high-grade zones are tectonically translated from different original stratigraphic levels and if the high grades were produced solely by this deformation. Nonetheless, the broad correspondence between high TOC and high P_2O_5 and Zn + Pb contents within the Duo Lake Formation raises the possibility that phosphate deposition and Zn-Pb mineralization in the district were linked in part to regional and global processes including high sea level and marine transgression.

Links to global anoxia

The Late Ordovician and Silurian are well known for global anoxic events (e.g., Page et al. 2007). Two especially long-lived events occurred from the late Ashgill to early Llandovery and from the late Llandovery to middle Wenlock (Fig. 11). The older anoxic event encompasses time periods during which strata of the Lower cherty member were deposited, including intervals in the upper part that contain very high TOC, P_2O_5, Mo, and V (Fig. 7); this event is also documented by trace element and stable isotope data in coeval strata elsewhere in the Selwyn Basin (Goodfellow et al. 1992; Wang et al. 1993) and globally (e.g., Melchin et al. 2013). Deposition of the Active member—characterized by low to high grades of Zn ± Pb and locally very high TOC contents—also took place entirely within this older anoxic event. The younger anoxic period encompasses deposition of the Upper siliceous mudstone member and in particular intervals that have the highest TOC and P_2O_5 contents. Global anoxia in the oceans can be fundamentally important in forming CD Pb Zn deposits by providing a source of abundant H_2S and by preventing the oxidation of sulphides on the sea floor due to an absence of dissolved O_2 (e.g., Goodfellow 1987; Turner 1992). Phosphogenesis is linked to anoxia by phosphorous release (regeneration) into bottom waters in

shallow sediments (Van Cappellen and Ingall 1994). Moreover, on continental shelves, the precipitation of apatite from aqueous phosphate by large sulphur bacteria is catalyzed most efficiently under anoxic bottom waters (Goldhammer et al. 2010).

Environments of phosphate and Zn-Pb mineralization

Previous models for the sedimentary environment of the numerous Zn-Pb deposits in the Howards Pass district have invoked long-lived and isolated anoxic subbasins within the Selwyn Basin (e.g., Goodfellow and Jonasson 1986; Goodfellow 2007). In contrast, our study suggests that local strata in the district record the transition from a basinal setting to an upper slope or outer shelf setting, and that the deposits formed in a single basin or trough rather than in separate depositional centers. In the following sections, we integrate whole-rock geochemical data from the Duo Lake Formation with results from modern sedimentary realms to build a comprehensive model for the setting and origin of phosphate and Zn-Pb deposits in the district.

Constraining the environment of mineralization requires an evaluation of diverse types of data from sedimentology, mineralogy, and geochemistry. Certain features of the lithostratigraphy within the district warrant discussion. One is the presence of thin limestone beds, which are especially widespread in the upper part of the Lower cherty mudstone and at the base of the Active member. These limestone beds are interpreted as distal carbonate turbidites, and as such likely reflect erosion of shallow-water carbonates on the shelf (Mackenzie platform; Fig. 1). A second important feature is the first appearance of phosphorites in the upper part of the Lower cherty member, extending into the lowermost part of the Active member. Third is the widespread occurrence of thin phosphate laminae within the Upper siliceous mudstone member. It is noteworthy that phosphate-rich strata occur regionally in the Duo Lake Formation, including samples that have up to 10.9 wt% P_2O_5 (Goodfellow et al. 1992; Fischer 2014); hence, phosphate concentrations within this formation are not limited to strata of the Howards Pass district.

Phosphate deposition

The distinctive phosphorite unit at the top of the Upper cherty member is fundamentally important to reconstructing the sedimentary environment. Phanerozoic and modern phosphorites form mainly by the upwelling of P-rich waters onto outer shelves or upper slopes of continental margins (e.g., Föllmi 1996; Trappe 1998; Arning et al. 2009b; Pufahl 2010). Phosphate can also accumulate by non-upwelling processes including within anoxic basins (Ruttenberg and Berner 1993); thus, it is critical to differentiate between these two potential settings for the phosphorite unit in the Duo Lake Formation.

Phosphate deposition in modern anoxic settings is well represented by occurrences in the Baltic Sea in waters more than ~100 m deep (Jilbert and Slomp 2013). This process involves a Fe-Mn-P shuttle in which HPO_4^{2-} is adsorbed onto ferric oxyhydroxide particles derived from shallow oxic waters of the shelf (Dellwig et al. 2010). Deposition of sparse apatite (or francolite) occurs in anoxic sediments via dissolution-reprecipitation mechanisms (März et al. 2008). Initial precipitation involves P-bearing ferric oxyhydroxide(s) followed by reduction to the hydrous iron phosphate vivianite [$Fe_3^{2+}(PO_4)_2 \bullet 8H_2O$] (Jilbert and Slomp 2013; Dijkstra et al. 2016). The early ferric oxyhydroxide-phosphate phase in the modern Baltic Sea has Fe/P ratios of 2.0 to 2.9 (Dellwig et al. 2010); the reduced—possibly transitory—phase has Fe/P close to the ratio of 1.5 for vivianite (Jilbert and Slomp 2013). These high Fe/P ratios contrast with the uniformly low ratios of 0.03 to 0.17 (avg 0.11 ± 0.05; $n = 6$) determined for phosphorites (>18 wt% P_2O_5) in the upper part of the Lower cherty member and with the similarly low Fe/P ratios of 0.09 to 0.45 (avg 0.30 ± 0.14; $n = 5$) that characterize P-rich (>5 wt% P_2O_5) and carbonate-poor mudstone intervals of the Upper siliceous mudstone member (Supplementary Data Table 1). Significantly, phosphorites from the modern Peruvian shelf also have low Fe/P ratios (0.03 to 0.14; avg. 0.05 ± 0.03, $n = 13$) as calculated from the data in Arning et al. (2009b). Thus, on the basis of bulk Fe/P ratios, both phosphatic intervals in the Duo Lake Formation are analogous to modern phosphorites of the Peruvian shelf, but are very different from modern phosphate occurrences in anoxic parts of the Baltic Sea. Additional relevant points are that no phosphate-rich strata are known within the Baltic Sea, and that true phosphorites are unlikely to form in such anoxic basins because the Fe-Mn-P shuttle probably cannot generate large concentrations of phosphate (see Jilbert and Slomp 2013). In conclusion, these arguments support a model in which the phosphatic intervals of the Duo Lake Formation formed by an upwelling process.

Upwelling on modern continental margins involves the movement of deep, nutrient- and P-rich waters into shallow shelf settings where biological and sedimentary processes generate fluorapatite and francolite concentrations (e.g., Föllmi 1996). In modern settings, this process preferentially occurs in subtropical (~15–30°) latitudes, as meridional (east-west) or alternatively Ekman (north-south) upwelling (Parrish 1982). During the Ordovician and Silurian, the northwestern margin of Laurentia was positioned north of the equator at similar latitudes (Torsvik and Cocks 2013) and hence was amenable to both types of marine upwelling (see Pope and Steffen 2003; Servais et al. 2014). During deposition of the Duo Lake phosphorites in the Late Ordovician (Hirnantian, based on a Rhuddanian age for the overlying Active member), upwelling was likely related to thermohaline circulation driven by contemporaneous and widespread glaciation (Pope and

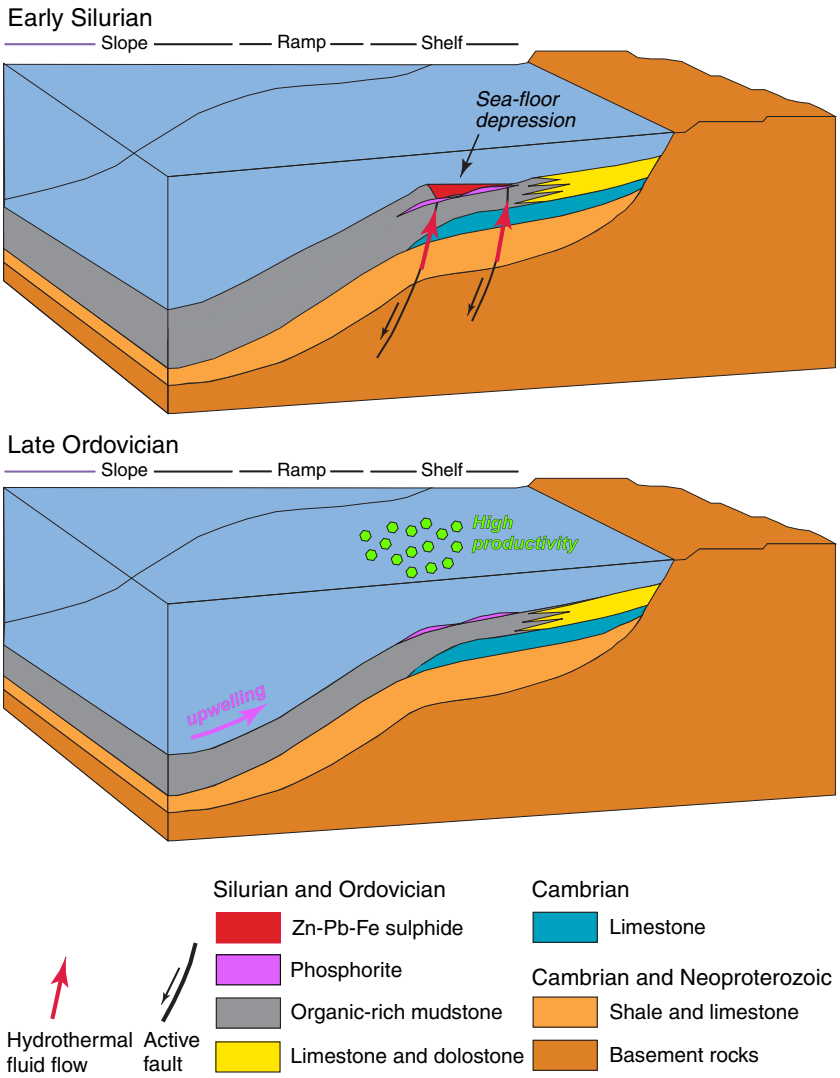

Fig. 12 Model for sedimentary environment during early Paleozoic formation of stratiform phosphate and Zn-Pb deposits in Howards Pass district. Views are along northwest strike of the district, approximately parallel to present edge of Mackenzie platform (Fig. 1). *Bottom*, Late Ordovician deposition of phosphorite in upper part of Lower cherty mudstone member, involving upwelling of nutrient- and P-rich waters onto outer shelf. *Top*, early Silurian deposition of Zn-Pb sulphides in Active member, within elongate sea-floor depression. Inferred growth faults are projected into Proterozoic basement rocks based on radiogenic isotope data (Cousens 2007). During middle Silurian time, deposition of phosphatic mudstone resumed in Upper siliceous mudstone member (see text)

Steffen 2003). Based on data from inferred modern analogs, the phosphate-rich sediments were deposited during brief periods of marine transgression and sea-level highstands in relatively shallow waters (<200 m) on upper slope or outer shelf settings (Föllmi 1996; Trappe 1998).

Textures of the phosphorites and phosphatic mudstones of the Duo Lake Formation indicate reworking on the sea floor and the local formation of hardgrounds. In the Upper cherty member, phosphorite samples have abundant clastic grains of fluorapatite-francolite (Fig. 6b–d) that are similar to those of modern reworked phosphorite deposits (e.g., Föllmi 1996; Trappe 1998; Pufahl 2010), in which phosphate concentration occurs by winnowing and reworking in a shallow shelf environment. In the Upper siliceous mudstone member, phosphate laminae appear homogeneous in hand sample (Fig. 5b) and under the microscope, but at high resolution via SEM these laminae show distinctive clastic textures (Fig. 6a) that support deposition by reworking of pre-existing phosphate accumulations. The thin phosphate laminae and the enclosing organic-rich black mudstone are remarkably similar in appearance to phosphatic mudstone within the Miocene Monterey Formation of coastal California, attributed by Föllmi et al. (2005) to condensed strata that record both primary and early diagenetic phosphogenesis on and near the sea floor. Based on studies of modern phosphate accumulation on the Peruvian and Namibian shelves, it is likely that deposition of phosphorites and phosphatic laminae in the Duo Lake Formation involved bacteria including anoxic sulphide-oxidizing bacteria

(Cosmidis et al. 2013, and references therein). A hydrothermal origin for the district phosphate proposed by Goodfellow and Jonasson (1986) and Goodfellow (2007) is ruled out by the above stratigraphic and sedimentological arguments and by in situ trace element and REE data for district apatite reported by Gadd et al. (2016a).

Basin to shelf transition in Duo Lake Formation

The stratiform Zn-Pb deposits of the Active member have long been attributed to syngenetic mineralization within separate anoxic basins or subbasins (Goodfellow and Jonasson 1986; Goodfellow 2007). However, the presence of phosphorites in the immediate footwall (Upper cherty member) and phosphatic mudstone in the hangingwall (Upper siliceous mudstone member) instead suggest a different environment, on an upper slope or outer shelf setting (Fig. 12). Geochemical support for this new model, in addition to the presence of locally high P_2O_5, includes a range of TOC, V, Mo, and U contents, and generally low Ce/Ce* values (Fig. 7), which collectively imply sulphidic to suboxic bottom waters that are typical of the dynamic redox environments of these settings (Brumsack 2006; Böning et al. 2009). Moreover, ratios of Mo/TOC × 10^{-4} for mudstone and phosphatic mudstone samples from the Lower cherty mudstone, Active, and Upper siliceous mudstone members are uniformly very low (avg 2.0 ± 1.9) like those of organic-rich sediments on the modern Namibian shelf (avg 6 ± 3), whereas Mo/TOC × 10^{-4} ratios of mudstones from the Pyritic and Calcareous members are relatively high (most ~12–20) and within the range of ratios for sediments of the modern anoxic Cariaco Basin (avg 25 ± 5), as compiled by Algeo and Lyons (2006). The major exception to this pattern is in sulphidic sediments of the Black Sea that have a low average Mo/TOC × 10^{-4} ratio of 4.5 ± 1, which reflects Mo limitation in the water column due to oceanographic isolation and lack of ventilation of the water column by Mo-bearing oxic seawater. However, a restricted Black Sea setting is considered unlikely for the middle and upper parts of the Duo Lake Formation owing to occurrence of the phosphorites and phosphatic mudstones, which require access to the open ocean for upwelling of nutrient- and P-rich waters and subsequent deposition of abundant phosphate.

The stratigraphic level of the proposed transition from a basin to an upper slope or outer shelf environment is suggested to be in the upper part of the Lower cherty mudstone member that was deposited in the Late Ordovician (Hirnantian). This member records a sharp drop in Mo/TOC × 10^{-4} ratios and contains phosphorite beds. In other ancient sedimentary successions of black shale and phosphorite, such as the phosphatic facies of the Permian Phosphoria Formation in the western USA, the phosphorites are thickest at the basin to slope transition (Tisoncik 1984) where upwelling P-rich waters preferentially impinged onto the continental shelf (Piper and Link 2002). This model is consistent with seaward migration of the shelf due to lowering of sea level during the preceding Hirnantian glaciation (Fig. 11) and with interpretations of migrating shelf facies in other ancient sedimentary successions (e.g., Plink-Björklund and Steel 2002; Bullimore et al. 2005). More work will be required to evaluate whether this model is applicable regionally to all of the Duo Lake Formation within the Selwyn Basin (e.g., Gordey and Anderson 1993).

Zn-Pb deposits

Based on the new model presented above, the Active member of the Duo Lake Formation and its contained Zn-Pb deposits formed in an upper slope or outer shelf setting (Fig. 12). Zn-Pb mineralization within separate anoxic (or sulphidic) basins is considered unlikely given multifaceted evidence from sedimentary lithofacies (e.g., widespread phosphorites) and geochemistry (e.g., Mo/TOC × 10^{-4} ratios). Owing to deformational overprints including locally pervasive thrust faults (Hodder et al. 2014), it is not feasible to discern primary seafloor topography during Zn-Pb mineralization in the Howards Pass district. However, if the modified model involving downward percolating dense metalliferous brine (Sangster 2002; Gadd et al. 2016b) is valid, then some type of seafloor depression is required in order to confine the brine and focus sulphide mineralization in the shallow subsurface. Given the similar lithofacies of the Duo Lake Formation that host the 15 different Zn-Pb deposits of the district (Kirkham et al. 2012), multiple depressions corresponding to each deposit are not required. Formation of the depression—or trough—may have been generated by synsedimentary faulting, which also was needed to produce conduits for metalliferous hydrothermal fluids to reach the sea floor. However, no evidence of such faulting—or a hydrothermal vent complex—is known in the district. Moreover, possible sedimentary products of synsedimentary faulting such as talus deposits or coarse sandstone have not been reported within the Duo Lake Formation, either locally within the district or regionally in the Selwyn Basin (Morganti 1979; Gordey and Anderson 1993). Nonetheless, some type of synsedimentary growth faulting likely occurred on the outer shelf (e.g., Gibbs 1984; McNeill et al. 1997) prior to and possibly during Zn-Pb mineralization, perhaps linked to sediment loading and drowning of the shelf. If the growth faults were small and lacked appreciable displacement, then they can be very difficult to recognize even in undeformed terranes (see Baudon and Cartwright 2008) and especially in shale-dominant sequences that lack marker beds. Although igneous rocks are unknown in district strata of the Duo Lake Formation, the presence of alkaline mafic volcanics in correlative early Silurian sequences of the Selwyn Basin (Fig. 11; Goodfellow et al. 1995) suggests that the hydrothermal system responsible for the Howards Pass Zn-Pb

deposits may have been driven by heat from mafic magmas at depth. However, magmatic heat is not required for the formation of most CD Zn-Pb deposits worldwide (Leach et al. 2005, and references therein), especially if fluids are infiltrated to at least ~3–5 km to attain elevated temperatures and effectively leach metals from source rocks at depth (e.g., Garven et al. 2003; Southgate et al. 2006).

In the modern marine realm, active sediment-hosted Zn-Pb mineralization is unknown and hence no direct analog exists for deposits of the Howards Pass district. However, some sites are similar in terms of sedimentology and general setting. For example, large depressions of diverse origin are well documented on outer parts of many continental shelves (e.g., Holtedahl 1958). The northeastern Atlantic shelf contains basins, channels, and troughs up to 400 km long and as much as 700 m deep (Uchupi 1968). On the Arctic shelf, glacially carved troughs 35 to 1400 km long, 12 to 260 km wide, and 200 to 1000 m deep have been delineated (Batchelor and Dowdeswell 2014). The early Silurian Active member at Howards Pass overlies Late Ordovician strata that are broadly coeval with the globally widespread Hirnantian glaciation (see Delabroye and Vecoli 2010; Finnegan et al. 2011). However, glacially carved troughs are unlikely analogs for the accumulation of the Zn-Pb deposits in the district because the host strata there, of Late Ordovician to early Silurian age, were deposited at low latitudes of ~10 to 20°N (Jin et al. 2013; Torsvik and Cocks 2013).

A viable candidate in the modern realm may be the Cariaco Basin on the continental shelf north of Venezuela. This elongate basin is ~200 km long, ~50 to 75 km wide, has a maximum depth of ~1400 m (below an interior saddle), and contains anoxic to sulphidic bottom waters (Peterson et al. 1991; Yarincik et al. 2000). A second potential modern analog is the Orca Basin in the southern Gulf of Mexico, which is ~30 km long and 500 to 700 m deep (below rim top) and has highly saline anoxic brines (Tribovillard et al. 2008); this basin is situated on the continental slope and not the shelf. Note, however, that a shelf- or slope-hosted basin is not favored for the Pyritic siliceous and Calcareous members because these lack phosphorous concentrations, which might be expected in such depositional settings; therefore, a basin external to the shelf and slope is preferred.

The previous consensus model for the Zn-Pb deposits of the district involves mineralization in multiple subbasins external to the Mackenzie carbonate platform (Goodfellow 2007 and references therein). Our studies argue against this model, based on evidence presented above for an outer shelf or upper slope setting for the Zn-Pb (and phosphate) deposits, but it may have relevance for the underlying members of the Duo Lake Formation (Fig. 3). A possible modern analog for the setting of these strata is in the so-called Southern California borderland. Here, west of the continental shelf and slope, eight silled basins ~10 to 100 km in diameter and up to ~1200 m deep (below sill top) contain suboxic to locally anoxic bottom waters (Gorsline 1990; Eichhubl et al. 2002). Two of these basins, Santa Barbara and Santa Monica, have diameters of ca. 40 to 50 km, similar to the present strike extent of the Zn-Pb deposits in the Howards Pass district (Fig. 2). This comparison is limited, however, by the fact that the Southern California borderland is an active continental margin, whereas CD Zn-Pb deposits typically form in passive margin settings (e.g., Leach et al. 2010).

Exploration applications

Results of this study have applications to mineral exploration on both local and regional scales. In addition to common geological, geochemical, and geophysical guides (e.g., Lavery et al. 1994; Goodfellow 2007), previous workers in the Howards Pass district have proposed the utility of diverse parameters including the presence of ammonium-rich mica (Williams et al. 1987), radiogenic Sr (Cousens 2007), and phengitic muscovite (Peter et al. 2015), among others. Our study provides a different perspective based on newly recognized sedimentary lithofacies and depositional settings for the Duo Lake Formation. Several findings are emphasized here. One is that two units of phosphorite and phosphate-rich black mudstone occur, respectively, stratigraphically below and above the Active member (Fig. 7). These phosphatic strata are not of hydrothermal origin, as suggested by Goodfellow and Jonasson (1986) and Goodfellow (2007), but instead are products of normal marine upwelling processes similar to those invoked for other ancient and modern phosphorites; this interpretation is supported by recently acquired trace element and REE data for apatite grains within the Howards Pass deposits and host rocks (Gadd et al. 2016a). A second key finding of our study is the unique depletion of LREE in sulphide-poor black mudstone of the Active member (Fig. 8), attributed here to the downward passage of dense and acidic metalliferous brines, which establishes an additional exploration guide.

A major conclusion presented here is that the phosphate and Zn-Pb deposits of the district formed within a single shallow depression in an upper slope or outer shelf setting and not in one or more marginal anoxic basins. This new model (Fig. 12) is based mainly on the stratigraphic distribution of phosphorite in the Upper cherty member below the Active member, and insights from modern analogs in which phosphorites form preferentially in these settings, where upwelling P-rich waters impinge on the continental shelf. This model implies that the exploration for Paleozoic CD Pb-Zn deposits elsewhere in the Selwyn Basin should include upper slope and outer shelf environments, close to and perhaps on the edge of the Mackenzie carbonate platform, as exemplified by the Late Silurian-Early Devonian Vulcan deposit (Fig. 1; Mako and Shanks 1984). As noted by Slack et al. (2015a), other stratiform sediment-hosted Zn-Pb deposits and prospects have stratigraphically associated phosphorites or apatite-rich beds including those in the Irecê area of Brazil (Kyle and Misi 1997; Misi et al. 2010), the Prades Mountains of Spain (Canet et al. 2004), and at the large Gamsberg orebody

in South Africa (Stalder and Rozendaal 2004). The Sekarna Zn-Pb deposit in Tunisia also has associated phosphatic strata (Garnit et al. 2012), but it is unclear whether this deposit has a CD Pb-Zn or MVT affinity. Significantly, some modern phosphorites have local concentrations of sphalerite, such as on the Peruvian shelf (Arning et al. 2009a). Collectively, these associations of Zn ± Pb deposits with phosphorites and phosphatic strata further support our model for Zn-Pb mineralization in the Howards Pass district having formed in an upper slope or outer shelf setting. This model has applications beyond the Selwyn Basin and hence may be applied to other ancient continental margin successions.

Acknowledgements This study was made possible through generous access to properties, drill cores, and exploration reports by Jason Dunning and the staffs of Selwyn Resources Ltd. and Selwyn Chihong Mining Ltd. Bob Hodder, Duncan Bain, and Edith Martel are thanked for geological guidance and David Legault and Matt Jodrey for help during core sampling. Suzanne Paradis supplied phosphorite-bearing drill cores for this study. Appreciation is also extended to USGS colleagues John Jackson for XRD data, Garth Graham for EMP analyses of apatite, and Harvey Belkin and Brett Valentine for SEM images; Julie Dumoulin provided petrographic data on limestones. Karl Föllmi supplied important field photographs of phosphatic strata in the Monterey Formation. Discussions with Craig Johnson and Julie Dumoulin have been helpful. The manuscript has been greatly improved by the comments and suggestions of USGS colleagues Clint Scott and Kate Whidden and by the detailed and constructive journal reviews of Mike Gadd, Thomas Monecke, and Elizabeth Turner.

Any use of trade, firm, or product names is for descriptive purposes only and does not imply endorsement by the U.S. Government.

References

Algeo TJ, Lyons TW (2006) Mo-total organic carbon covariation in modern anoxic marine environments: implications for analysis of paleoredox and paleohydrographic conditions. Paleoceanogr 21: PA1016. doi:10.1029/2004PA001112

Algeo TJ, Rowe H (2012) Paleoceanographic applications of trace-metal concentration data. Chem Geol 324-325:6–18

Ardakani OH, Chappaz A, Sanei H, Mayer B (2016) Effect of thermal maturity on remobilization of molybdenum in black shales. Earth Planet Sci Lett 449:311–320

Arning ET, Birgel D, Brunner B, Peckmann J (2009a) Bacterial formation of phosphatic laminites off Peru. Geobiol 7:295–307

Arning ET, Lückge A, Breuer C, Gussone N, Birgel D, Peckmann J (2009b) Genesis of phosphorite crusts off Peru. Mar Geol 262:68–81

Atlas E, Pytkowicz RM (1977) Solubility behavior of apatites in seawater. Limnol Oceanogr 22:290–300

Ayers JC, Watson EB (1991) Solubility of apatite, monazite, zircon, and rutile in supercritical aqueous fluids with implications for subduction zone geochemistry. Phil Trans Royal Soc London 335(A):365–375

Batchelor CL, Dowdeswell JA (2014) The physiography of high Arctic cross-shelf troughs. Quarter Sci Rev 92:68–96

Bau M, Dulski P (1996) Distribution of yttrium and rare-earth elements in the Penge and Kuruman iron-formations, Transvaal Supergroup, South Africa. Precamb Res 79:37–55

Baudon C, Cartwright J (2008) Early stage evolution of growth faults: 3D seismic insights from the Levant Basin, eastern Mediterranean. Jour Struct Geol 30:888–898

Berner RA, Raiswell R (1983) Burial of organic carbon and pyrite sulfur in sediments over Phanerozoic time: a new theory. Geochim Cosmochim Acta 47:855–862

Böning P, Brumsack H-J, Schnetger B, Grunwald M (2009) Trace element signatures of Chilean upwelling sediments at ~36°S. Mar Geol 259:112–121

Breit GN, Wanty RB (1991) Vanadium accumulation in carbonaceous rocks: a review of geochemical controls during deposition and diagenesis. Chem Geol 91:83–97

Broadbent GC, Myers RE, Wright JV (1998) Geology and origin of shale-hosted Zn-Pb-Ag mineralization at the Century deposit, northwest Queensland, Australia. Econ Geol 93:1264–1294

Brumsack H-J (2006) The trace metal content of recent organic carbon-rich sediments: implications for Cretaceous black shale formation. Palaeogeogr Palaeoclimatol Palaeoecol 232:344–361

Bullimore S, Henriksen S, Liestøl FM, Helland-Hansen W (2005) Clinoform stacking patterns, shelf-edge trajectories and facies associations in Tertiary coastal deltas, offshore Norway: implications for the prediction of lithology in prograding systems. Norwegian J Geol 85:169–187

Burdige DE (2006) Geochemistry of marine sediments. Princeton University Press, Princeton, 609 pp

Calner M (2008) Silurian global events—at the tipping point of climate change. In: Elewa AMT (ed) Mass extinction. Springer, Berlin-Heidelberg, pp. 21–57

Canet C, Alfonso P, Melgarejo JC, Belyatsky BV (2004) Geochemical evidences of sedimentary-exhalative origin of the shale-hosted PGE-Ag-Au-Zn-Cu occurrences of the Prades Mountains (Catalonia, Spain): trace element abundances and Sm-Nd isotopes. J Geochem Explor 82:17–33

Canfield DE, Thamdrup B, Hansen JW (1993) The anaerobic degradation of organic matter in Danish coastal sediments: iron reduction, manganese reduction, and sulfate reduction. Geochim Cosmochim Acta 57:3867–3883

Chaïrat C, Schott J, Oelkers EH, Lartigue J-E, Harouiya N (2007) Kinetics and mechanism of natural fluorapatite dissolution at 25°C and pH from 3 to 12. Geochim Cosmochim Acta 71:5901–5912

Chen J, Walter MR, Logan GA, Hinman MC, Summons RE (2003) The Paleoproterozoic McArthur River (HYC) Pb/Zn/Ag deposit of northern Australia: organic geochemistry and ore genesis. Earth Planet Sci Lett 210:467–479

Cosmidis J, Benzerara K, Menguy N, Arning E (2013) Microscopy evidence of bacterial microfossils in phosphorite crusts of the Peruvian shelf: implications for phosphogenesis mechanisms. Chem Geol 359:10–22

Cousens BL (2007) Radiogenic isotope studies of Pb-Zn mineralization in the Howards Pass area, Selwyn Basin. Geol Surv Canada Open File 5344:279–292

Creaney S, Passey QR (1993) Recurring patterns of total organic carbon and source rock quality within a sequence stratigraphic framework. Amer Assoc Petrol Geol Bull 77:386–401

Delabroye A, Vecoli M (2010) The end-Ordovician glaciation and the Hirnantian stage: a global review and questions about Late Ordovician event stratigraphy. Earth-Sci Rev 98:269–282

Dellwig O, Leipe T, März C, Glockzin M, Pollehne F, Schnetger B, Yakushev EV, Böttcher ME, Brumsack H-J (2010) A new particulate Mn-Fe-P-shuttle at the redoxcline of anoxic basins. Geochim Cosmochim Acta 74:7100–7115

Dijkstra N, Slomp CP, Behrends T, Expedition 347 Scientists (2016) Vivianite is a key sink for phosphorus in sediments of the Landsort Deep, an intermittently anoxic deep basin in the Baltic Sea. Chem Geol 438:58–72

Eichhubl P, Greene HG, Maher N (2002) Physiography of an active transpressive margin basin: high-resolution bathymetry of Santa Barbara basin, Southern California borderland. Marine Geol 184: 95–120

Finnegan S, Bergmann K, Eiler JM, Jones DS, Fike DA, Eisenman I, Hughes NC, Tripati AK, Fischer WW (2011) The magnitude and duration of Late Ordovician-early Silurian glaciation. Science 331: 903–906

Fischer BJ (2014) Lithogeochemical analyses of rocks from the Selma project (Bonnet Plume River mapsheet NTS 106B; also 105O, 105P, and Howard's Pass in 105I). Northwest Territories Geoscience Office, Yellowknife, NWT Open Report 2014-008, 12 pp and digital files

Föllmi KB (1996) The phosphorus cycle, phosphogenesis and marine phosphate-rich deposits. Earth-Sci Rev 40:55–124

Föllmi KB, Badertscher C, de Kaenel E, Stille P, John CM, Adatte T, Steinmann P (2005) Phosphogenesis and organic-carbon preservation in the Miocene Monterey Formation at Naples Beach, California—the Monterey hypothesis revisited. Geol Soc Amer Bull 117:589–619

Gadd MG, Layton-Mathews D, Peter JM (2016a) Non-hydrothermal origin of apatite in SEDEX mineralization and host rocks of the Howard's Pass district. Yukon, Canada: Amer Min 101:1061–1071

Gadd MG, Layton-Mathews D, Peter JM, Paradis SJ (2016b) The world-class Howard's Pass SEDEX Zn-Pb district, Selwyn Basin, Yukon. Part I: trace element compositions of pyrite record input of hydrothermal, diagenetic, and metamorphic fluids to mineralization. Mineral Deposita 51:319–342

Gadd MG, Layton-Mathews D, Peter JM, Paradis S, Jonasson IR (2016c) The world-class Howard's Pass SEDEX Zn-Pb district, Selwyn Basin, Yukon. Part II: the roles of thermochemical and bacterial sulfate reduction in metal fixation. Mineral Deposita. doi:10.1007/s00126-016-0672-x

Garnit H, Bouhlel S, Barca D, Johnson CA, Chtara C (2012) Phosphorite-hosted zinc and lead mineralization in the Sekarna deposit (central Tunisia). Mineral Deposita 47:545–562

Garven G, Raffensperger JP, Dumoulin JA, Bradley DA, Young LE, Kelley KD, Leach DL (2003) Coupled head and fluid flow modeling of the Carboniferous Kuna Basin, Alaska: implications for the genesis of the Red Dog Pb-Zn-Ag-Ba ore district. J Geochem Expl 78-79:215–219

Ghienne J-F, Desrochers A, Vandenbroucke TRA, Achab A, Asselin E, Dabard M-P, Farley C, Loi A, Paris F, Wickson S, Veizer J (2014) A Cenozoic-style scenario for the end-Ordovician glaciation. Nature Commun 5. doi:10.1038/ncomms5485

Gibbs AD (1984) Structural evolution of extensional basin margins. J Geol Soc London 141:609–620

Goldhammer T, Brüchert V, Ferdelman T, Zabel M (2010) Microbial sequestration of phosphorus in anoxic upwelling sediments. Nature Geosci 3:557–561

Goodfellow WD (1984) Geochemistry of rocks hosting the Howards Pass (XY) strata-bound Zn-Pb deposit, Selwyn Basin, Yukon Territory, Canada. In: Janelidze TV, Tvalchrelidze AG (eds) Proceed Sixth Quad IAGOD Symp. E Schweizerbart'sche Verlagsbuchhandlung, Stuttgart, pp. 91–112

Goodfellow WD (1987) Anoxic stratified oceans as a source of sulphur in sediment-hosted stratiform Zn-Pb deposits (Selwyn Basin, Yukon, Canada). Chem Geol 65:359–382

Goodfellow WD (2000) Anoxic conditions in the Aldridge Basin during formation of the Sullivan Zn-Pb deposit: implications for the genesis of massive sulphides and distal hydrothermal sediments. In: Lydon JW, Höy T, Slack JF, Knapp ME (eds) The geological environment of the Sullivan deposit, British Columbia, Geol Assoc Canada, Miner Deposits Div Spec Publ 1, pp. 218–250

Goodfellow WD (2007) Base metal metallogeny of the Selwyn Basin, Canada. In: Goodfellow WD (ed) Mineral deposits of Canada: a synthesis of major deposit types, district metallogeny, the evolution of geological provinces, and exploration methods, Geol Assoc Canada, Miner Deposits Div Spec Publ, vol 5, pp. 553–579

Goodfellow WD, Jonasson IR (1986) Environment of formation of the Howards Pass (XY) Zn-Pb deposit, Selwyn Basin, Yukon. In: Morin JA (ed) Mineral deposits of northern Cordillera, Canad Inst Mining Metall Spec, vol 37, pp. 19–50

Goodfellow WD, Jonasson IR, Morganti JM (1983) Zonation of chalcophile elements about the Howard's Pass (XY) Zn-Pb deposit, Selwyn Basin, Yukon. J Geochem Expl 19:503–542

Goodfellow WD, Nowlan GS, McCracken AD, Lenz AC, Grégoire DC (1992) Geochemical anomalies near the Ordovician-Silurian boundary, northern Yukon Territory, Canada. Historical Biol 6:1–23

Goodfellow WD, Cecile MP, Leybourne MI (1995) Geochemistry, petrogenesis, and tectonic setting of lower Paleozoic alkalic and potassic volcanic rocks, northern Canadian Cordilleran miogeocline. Canad Jour Earth Sci 32:1236–1254

Gordey SP, Anderson RG (1993) Evolution of the northern Cordilleran miogeocline, Nahanni map area (105I), Yukon and Northwest Territories. Geol Surv Canada Mem 428, 214 pp

Gorsline DS (1990) Controls on deep marine sedimentation. In: Brown GC, Gorsline DS, Schweller WJ (eds) Deep-marine sedimentation: depositional models and case histories in hydrocarbon exploration and development, Pacific Section Soc Econ Paleontol Mineral, Bakersfield, Calif., Short Course, vol 66, pp. 23–51

Gradstein FM, Ogg JG, Schmitz MD, Ogg GM (2012) The geologic time scale 2012. Elsevier, Amsterdam, 1144 pp

Hanor JS (1996) Controls on the solubilization of lead and zinc in basinal brines. In: Sangster DF (ed) Carbonate-hosted lead-zinc deposits, Society Economic Geologists Spec Publ, vol 4, pp. 483–500

Hodder R, Bain DJ, Martel E (2014) Interpretive structural geology map and cross-sections of the Howard's Pass Pb-Zn district, Yukon and Northwest Territories. Northwest Territories Geoscience Office, NWT Open File 2014–02, scale 1:50,000, one sheet and digital files

Holtedahl H (1958) Some remarks on geomorphology of continental shelves off Norway, Labrador, and southeast Alaska. J Geol 66: 461–471

Jilbert T, Slomp CP (2013) Iron and manganese shuttles control the formation of authigenic phosphorous minerals in the euxinic basins of the Baltic Sea. Geochim Cosmochim Acta 107:155–169

Jin J, Harper DAT, Cocks LRM, McCausland PJA, Rasmussen CMØ, Sheehan PM (2013) Precisely locating the Ordovician equator in Laurentia. Geology 41:107–110

Johnson CA, Slack JF, Falck H, Kelley KD (2014) Depositional environment of mudstone host rocks at the Howards Pass Zn-Pb deposits, Yukon Territory, Canada: insights from Fe speciation, S isotopes, and Fe/Al and Mo/TOC ratios. Geol Soc Amer Abs Pgms 46(6):250

Johnson CA, Dumoulin JA, Buruss RA, Slack JF (2015) Depositional conditions for the Kuna Formation, Red Dog Zn-Pb-Ag-barite district, Alaska, inferred from isotopic and chemical proxies. Econ Geol 110:1143–1156

Jonasson IR, Goodfellow WD (1986) Sedimentary and diagenetic textures, and deformation structures within the sulphide zone of the Howards Pass (XY) Zn-Pb deposit, Yukon and Northwest Territories. In: Morin JA (ed) Mineral deposits of northern ordillera, Canad Inst Mining Metall Spec, vol 37, pp. 51–70

Kelley KD, Dumoulin JA, Jennings S (2004a) The Anarraaq Zn-Pb-Ag and barite deposit, northern Alaska: evidence for replacement of carbonate by barite and sulfides. Econ Geol 99:1577–1591

Kelley KD, Leach DL, Johnson CA, Clark JL, Fayek M, Slack JF, Anderson VM, Ayuso RA, Ridley WI (2004b) Textural, compositional, and sulfur isotope variations of sulfide minerals in the Red Dog Zn-Pb-Ag deposits, Brooks Range, Alaska, USA: implications for ore formation. Econ Geol 99:1509–1532

Kelley KD, Selby D, Falck H, Slack JF (2016) Re-Os systematics of pyrite associated with Zn-Pb mineralization in the Howards Pass

area, Yukon and Northwest Territories, Canada. Miner Deposita. doi:10.1007/s00126-016-0663-y

Ketris MP, Yudovich YE (2009) Estimations of Clarkes for carbonaceous biolithes: world averages for trace element contents in black shales and coals. Inter J Coal Geol 78:135–148

Kirkham G, Dunning J, Schleiss W (2012) Update for Don deposit mineral resource estimate, Howard's Pass property, eastern Yukon: NI 43-101 Technical Rept. Available at: www.sedar.com

Krauskopf KB, Bird DK (1995) Introduction to geochemistry, 3rd edn. McGraw-Hill, New York, 647 pp

Kříbek B (1991) Metallogeny, structural, lithological and time controls of ore deposition in anoxic environments. Mineral Deposita 26:122–131

Kyle JR, Misi A (1997) Origin of Zn-Pb-Ag sulfide mineralization within Upper Proterozoic phosphate-rich carbonate strata, Irec Basin, Bahia, Brazil. Inter Geol Rev 39:383–399

Lavery NG, Leach DL, Saunders JA (1994) Lithogeochemical investigations applied to exploration for sediment-hosted lead-zinc deposits. In: Fontboté L, Boni M (eds) Sediment-hosted Zn-Pb ores, Soc Geol Applied Min Deposits Spec Publ, vol 10, pp. 393–428

Leach DL, Sangster DF, Kelley KD, Large RR, Garven G, Allen CR, Gutzmer J, Walters S (2005) Sediment-hosted lead-zinc deposits—a global perspective. In: Hedenquist JW, Thompson JFH, Goldfarb RJ, Richards JP (eds) Economic Geology 100th Anniversary Volume, 1905-2005. Society of Economic Geologists, Inc., Littleton, Colorado, pp. 561–607

Leach DL, Bradley DC, Huston D, Pisarevsky SA, Taylor RD, Gardoll SJ (2010) Sediment-hosted lead-zinc deposits in Earth history. Econ Geol 105:593–625

Lenz AC (1982) Ordovician to Devonian sea-level changes in western and northern Canada. Canad J Earth Sci 19:1919–1932

Lottermoser BG (1992) Rare earth elements and hydrothermal ore formation processes. Ore Geol Rev 7:25–41

Lowe DR (1982) Sediment gravity flows; II. Depositional models with special reference to the deposits of high-density turbidity currents. J Sed Petrol 52:279–297

Loydell DK (1998) Early Silurian sea-level changes. Geol Mag 135:447–471

Lyons TW, Severmann S (2006) A critical look at iron paleoredox proxies: new insights from modern euxinic marine basins. Geochim Cosmochim Acta 70:5698–5722

Lyons TW, Werne JP, Hollander DJ, Murray RW (2003) Contrasting sulfur geochemistry and Fe/Al and Mo/Al ratios across the last oxic-to-anoxic transition in the Cariaco Basin, Venezuela. Chem Geol 195:131–157

Magnall JM, Gleeson SA, Stern RA, Newton RJ, Poulton SW, Paradis S (2016) Open system sulphate reduction in a diagenetic environment—isotopic analysis of barite ($\delta^{34}S$ and $\delta^{18}O$) and pyrite ($\delta^{34}S$) from the Tom and Jason Late Devonian Zn-Pb-Ba deposits, Selwyn Basin, Canada. Geochim Cosmochim Acta 180:146–163

Mako DA, Shanks WCIII (1984) Stratiform sulfide and barite-fluorite mineralization of the Vulcan prospect, Northwest Territories: exhalation of basinal brines along a faulted continental margin. Canad Jour Earth Sci 21:78–91

Martel E (2015) The structural model for Howard's Pass Pb-Zn district, Northwest Territories: grounds for re-interpretation. Northwest Territories Geol Survey Open File, 2015–01, 54 pp

März C, Poulton SW, Beckmann B, Küster K, Wagner T, Kasten S (2008) Redox sensitivity of P cycling during marine black shale formation: dynamics of sulfidic and anoxic, non-sulfidic bottom waters. Geochim Cosmochim Acta 72:3703–3717

McClay KR (1991) Deformation of stratiform Zn-Pb(-barite) deposits in the northern Canadian Cordillera. Ore Geol Rev 6:435–462

McClellan GH, Van Kauwenbergh SJ (1990) Mineralogy of sedimentary apatites. In: Notholt AJG, Jarvis I (eds) Phosphorite research and development, Geol Soc Spec Publ, vol 52, pp. 23–31

McCracken AD (2014) Report on conodont samples from the District of Mackenzie, Northwest Territories. Geol Survey Canada Paleon Rept 05-ADM-2013, 25 pp

McLennan SM (1989) Rare earth elements in sedimentary rocks: influence of provenance and sedimentary processes. Rev Mineral 21: 169–200

McNeill LC, Piper KA, Goldfinger C, Kulm LD, Yeats RS (1997) Listric normal faulting on the Cascadia continental margin. Jour Geophys Res 102(B):12,123–12,138

Melchin MJ, Mitchell CE, Holmden C, Štorch P (2013) Environmental changes in the Late Ordovician-early Silurian: review and new insights from black shales and nitrogen isotopes. Geol Soc Amer Bull 125:1635–1670

Misi A, Azmy K, Kaufman AJ, Oliveira TF, Pinho JM, Sanches AL (2010) Metallogenic and phosphogenic events in the cratonic and passive-margin Proterozoic basins of the São Francisco craton: the Bambuí/Una and Vazante Groups. Proceed VII South American Symp Isotope Geol, Brasília, 25–28 July 2010, 4 pp

Morganti JM (1979) The geology and ore deposits of the Howard's Pass area, Yukon and Northwest Territories: the origin of basinal sedimentary stratiform sulfide deposits. Unpub PhD thesis, University of British Columbia, Vancouver, 317 pp

Mortlock RA, Froelich PN, Feely RA, Massoth GJ, Butterfield DA, Lupton JE (1993) Silica and germanium in Pacific Ocean hydrothermal vents and plumes. Earth Planet Sci Lett 119:365–378

Munnecke A, Calner M, Harper DAT, Servais T (2010) Ordovician and Silurian sea-water chemistry, sea level, and climate: a synopsis. Palaeogeogr Palaeoclimatol Palaeoecol 296:389–413

Norford BS, Orchard MJ (1985) Early Silurian age of rocks hosting lead-zinc mineralization at Howards Pass, Yukon Territory and District of MacKenzie; local biostratigraphy of Road River Formation and Earn Group. Geol Survey Canada Paper, 83–18, 35 pp

Ootes L, Gleeson SA, Turner E, Rasmussen K, Gordey S, Falck H, Martel E, Pierce K (2013) Metallogenic evolution of the Mackenzie and eastern Selwyn Mountains of Canada's northern Cordillera, Northwest Territories: a compilation and review. Geosci Canada 40:40–69

Page AA, Zalasiewicz JA, Williams M, Popov LE (2007) Were transgressive black shales a negative feedback modulating glacioeustasy in the early Palaeozoic icehouse? In: Williams M, Haywood AM, Gregory FJ, Schmidt DN (eds) Deep-time perspectives on climate change: marrying the signal from computer models and biological proxies, Geol Soc London Micropalaeon Soc Spec Publ, pp. 123–156

Parrish JT (1982) Upwelling and petroleum source beds, with reference to the Paleozoic. Amer Assoc Petrol Geol Bull 66:750–774

Peter JM, Layton-Matthews D, Gadd MG, Gill S, Baker S, Plett S, Paradis S (2015) Application of visible-near infrared and short wave infrared spectroscopy to sediment-hosted zinc-lead deposit exploration in the Selwyn Basin, Yukon. Geol Surv Canada Open File 7838: 152–172

Peterson LC, Overpeck JT, Kipp NG, Imbrie J (1991) A high-resolution late Quarternary upwelling record from the anoxic Cariaco Basin, Venezuela. Paleoceanogr 6:99–119

Piper DZ, Link PK (2002) An upwelling model for the Phosphoria sea: a Permian, ocean-margin sea in the northwest United States. AAPG Bull 86:1217–1235

Plink-Björklund P, Steel R (2002) Sea-level fall below the shelf edge, without basin-floor fans. Geology 30:115–118

Pope MC, Steffen JB (2003) Widespread, prolonged late Middle to Late Ordovician upwelling in North America: a proxy record of glaciation? Geology 31:63–66

Pufahl PK (2010) Bioelemental sediments. In: James NP, Dalrymple RW (eds) Facies models, Geol Assoc Canada, 4th edn, pp. 477–503

Rejebian VA, Harris AG, Huebner JS (1987) Conodont color and textural alteration: an index to regional metamorphism, contact

metamorphism, and hydrothermal alteration. Geol Soc Amer Bull 99:471–479

Ross DJK, Bustin RM (2009) Investigating the use of sedimentary geochemical proxies for paleoenvironment interpretation of thermally mature organic-rich strata: examples from the Devonian-Mississippian shales, western Canada sedimentary basin. Chem Geol 260:1–19

Ruttenberg KC, Berner RA (1993) Authigenic apatite formation and burial in sediments from non-upwelling, continental margin environments. Geochim Cosmochim Acta 57:991–1007

Sáez R, Moreno C, González F, Almodóvar GR (2011) Black shales and massive sulfide deposits: causal or casual relationships? Insights from Rammelsberg, Tharsis, and Draa Sfar. Mineral Deposita 46: 585–614

Sangster D (2002) The role of dense brines in the formation of vent-distal sedimentary-exhalative (SEDEX) lead-zinc deposits: field and laboratory evidence. Mineral Deposita 37:149–157

Scott C, Lyons TW (2012) Contrasting molybdenum cycling and isotopic properties in euxinic versus non-euxinic sediments and sedimentary rocks: refining the paleoproxies. Chem Geol 324-325:19–27

Scott C, Slack JF, Kelley KD (2013) The origin of vanadium hyperenriched black shales. Geol Soc Amer Abs Pgms 45(7):427

Servais T, Danelian T, Alexander D, Harper T, Munnecke A (2014) Possible oceanic circulation patterns, surface water currents and upwelling zones in the early Paleozoic. GFF [Geologiska Föreningen] 136:229–233

Slack JF, Dumoulin JA, Schmidt JM, Young LE, Rombach CS (2004a) Paleozoic sedimentary rocks in the Red Dog Zn-Pb-Ag district and vicinity, western Brooks Range, Alaska: provenance, deposition, and metallogenic significance. Econ Geol 99:1385–1414

Slack JF, Kelley KD, Anderson VM, Clark JL, Ayuso RA (2004b) Multistage hydrothermal silicification and Fe-Tl-As-Sb-Ge-REE enrichment in the Red Dog Zn-Pb-Ag district, northern Alaska: geochemistry, origin, and exploration applications. Econ Geol 99:1481–1508

Slack JF, Grenne T, Bekker A (2009) Seafloor-hydrothermal Si-Fe-Mn exhalites in the Pecos greenstone belt, New Mexico, and the redox state of ca. 1720 Ma deep seawater. Geosphere 5:302–314

Slack JF, Falck H, Dumoulin JD (2015a) Outer shelf and slope settings for sediment-hosted stratiform Zn-Pb deposits: evidence from associated phosphorites and phosphate-rich strata. Geol Soc Amer Abs Pgms 47(7):815

Slack JF, Rosa D, Falck H (2015b) Oxic to anoxic transition in bottom waters during formation of the Citronen Fjord sediment-hosted Zn-Pb deposit, North Greenland. In: André-Mayer A-S, Cathelineau M, Muehez P, Piraid E, Sindern S (eds) Mineral resources in a sustainable world: Proceed 13th Biennial SGA Mtg, Nancy, France, vol 5, pp. 2013–2016

Slack JF, Selby D, Dumoulin JA (2015c) Hydrothermal, biogenic, and seawater components in metalliferous black shales of the Brooks Range, Alaska: synsedimentary metal enrichment in a carbonate ramp setting. Econ Geol 110:653–675

Southgate PN, Kyser TK, Scott DL, Large RR, Golding SD, Polito PA (2006) A basin system and fluid-flow analysis of the Zn-Pb-Ag Mount Isa-type deposits of northern Australia: identifying metal source, basinal brine reservoirs, times of fluid expulsion, and organic matter reactions. Econ Geol 101:1103–1115

Stalder M, Rozendaal A (2004) Apatite nodules as an indicator of depositional environment and ore genesis for the Mesoproterozoic Broken Hill-type Gamsberg Zn-Pb deposit, Namaqua Province, South Africa. Mineral Deposita 39:189–203

Stock MJ, Humphreys MCS, Smith VC, Johnson RD, Pyle DM, EIMF (2015) New constraints on electron-beam induced halogen migration in apatite. Amer Mineral 100:281–293

Sverjensky DA (1984) Europium redox equilibria in aqueous solution. Earth Planet Sci Lett 67:70–78

Taylor SR, McLennan SM (1985) The continental crust: its composition and evolution. Blackwell Scientific Publications, Oxford, 312 pp

Tisoncik DD (1984) Regional lithostratigraphy of the Phosphoria Formation in the overthrust belt of Wyoming, Utah and Idaho. In: Woodward J, Meissner FF, Clayton JL (eds) Hydrocarbon source rocks of the greater Rocky Mountain region, Rocky Mountain Assoc Geol, pp. 295–320

Torsvik TH, Cocks LRM (2013) New global palaeogeographical reconstructions for the lower Palaeozoic and their generation. In: Harper DAT, Servias T (eds) Early Palaeozoic biogeography and geography, Geol Soc London Mem, vol 38, pp. 5–24

Trappe J (1998) Phanerozoic phosphorite depositional systems—a dynamic model for a sedimentary resource system, Lecture Notes in Earth Sci, vol 76. Springer, Berlin, 316 pp

Tribovillard N, Algeo T, Lyons T, Riboulleau A (2006) Trace metals as paleoredox and paleoproductivity proxies: an update. Chem Geol 232:12–32

Tribovillard N, Bout-Roumazeilles V, Algeo T, Lyons TW, Sionneau T, Montero-Serrano JC, Riboulleau A, Baudin F (2008) Paleodepositional conditions in the Orca Basin as inferred from organic matter and trace metal contents. Marine Geol 254:62–72

Turner RJW (1992) Formation of Phanerozoic stratiform sediment-hosted zinc-lead deposits: evidence for the critical role of ocean anoxia. Chem Geol 99:165–188

Uchupi E (1968) Atlantic continental shelf and slope of the United States—physiography. US Geol Survey Prof Paper 529-C, 30 pp

Van Cappellen P, Ingall E (1994) Benthic phosphorus regeneration, net primary production, and ocean anoxia: a model of the coupled marine biogeochemical cycles of carbon and phosphorus. Paleoceanogr 9:677–692

Wang K, Chatterton BDE, Attrep M Jr, Orth CJ (1993) Late Ordovician mass extinction in the Selwyn Basin, northwestern Canada: geochemical, sedimentological, and paleontological evidence. Can J Earth Sci 30:1870–1880

Wignall PB (1994) Black shales. Oxford Monographs Geol Geophys 30, 27 pp

Wignall PB, Newton R (1998) Pyrite framboid diameter as a measure of oxygen deficiency in ancient mudrocks. Amer Jour Sci 298:537–552

Wilkin RT, Arthur MA, Dean WE (1997) History of water-column anoxia in the Black Sea indicated by pyrite framboid size distributions. Earth Planet Sci Lett 148:517–525

Wilkinson JJ (2014) Sediment-hosted zinc-lead mineralization: processes and perspectives. In: Scott SD (ed) Geochemistry of mineral deposits, Treatise on Geochemistry, vol 13, 2nd edn. Elsevier, Amsterdam, pp. 219–249

Williams LB, Zantop H, Reynolds RC (1987) Ammonium silicates associated with sedimentary exhalative ore deposits: a geochemical exploration tool. J Geochem Expl 27:125–141

Yarincik KM, Murray RW, Lyons TW, Peterson LC, Haug GH (2000) Oxygenation history of bottom waters in the Cariaco Basin, Venezuela, over the past 578,000 years: results from redox-sensitive metals (Mo, V, Mn, Fe). Paleoceanogr 15:593–604